

Banner appropriate to article type will appear here in typeset article

Attention on flow control: transformer-based reinforcement learning for lift regulation in highly disturbed flows

Zhecheng Liu and Jeff D. Eldredge

Mechanical and Aerospace Engineering, University of California, Los Angeles, CA 90095-1597, USA

(Received xx; revised xx; accepted xx)

A linear flow control strategy designed for weak disturbances may not remain effective in sequences of strong disturbances due to nonlinear interactions, but it is sensible to leverage it for developing a better strategy. In the present study, we propose a transformer-based reinforcement learning (RL) framework to learn an effective control strategy for regulating aerodynamic lift in gust sequences via pitch control. The transformer addresses the challenge of partial observability from limited surface pressure sensors. We demonstrate that the training can be accelerated with two techniques—pretraining with an expert policy (here, linear control) and task-level transfer learning (here, extending a policy trained on isolated gusts to multiple gusts). We show that the learned strategy outperforms the best proportional control, with the performance gap widening as the number of gusts increases. The control strategy learned in an environment with a small number of successive gusts is shown to effectively generalize to an environment with an arbitrarily long sequence of gusts. We investigate the pivot configuration and show that quarter-chord pitching control can achieve superior lift regulation with substantially less control effort compared to mid-chord pitching control. Through a decomposition of the lift, we attribute this advantage to the dominant added-mass contribution accessible via quarter-chord pitching. The success on multiple configurations shows the generalizability of the proposed transformer-based RL framework, which offers a promising approach to solve more computationally demanding flow control problems when combined with the proposed acceleration techniques.

Key words:

1. Introduction

An interest in large manned air vehicles has been extended to encompass unmanned air vehicles (UAVs) in recent years, particularly to serve roles in intelligence, surveillance, and delivery (Laghari *et al.* 2023). When performing a wide range of operations, it is expected for UAVs to achieve stable flight even in extreme environments where they may encounter sizable atmospheric disturbances (gusts) (Fukami & Taira 2023). However, a large force and moment transient experienced during gust encounters may impact the flight path and safety of the aircraft and, over time, cause structural fatigue to the vehicle (Wu *et al.* 2019).

Abstract must not spill onto p.2

Therefore, many recent studies have been devoted to investigating the underlying unsteady aerodynamic physics of gust encounters (Eldredge & Jones 2019; Jones *et al.* 2022; Narayanan & Govindarajan 2024) and designing control strategies to mitigate gust effect (Oduyela & Slegers 2014; Sedky *et al.* 2022; Kerstens *et al.* 2011).

Each combination of the control objectives (e.g., separation prevention, lift enhancement, or drag reduction), actuation methods (e.g., pitching, control surface, or synthetic jets), and the availability of measurements (e.g., pressure, velocity, acceleration, or force and moment), presents unique challenges and requires a tailored design approach. The control problem is manageable when gusts are of small amplitude, so that one can rely on linear control theory designed on a linear model of the aerodynamics. For example, Sedky *et al.* (2022) designed a controller to mitigate the lift variation on an airfoil by modeling the lift response to pitching kinematics and transverse gust from the superposition of the classical Küssner model (Küssner 1932) and Wagner model (Wagner 1925). Brunton & Rowley (2013) developed an empirical state-space form of Theodorsen model (Theodorsen 1949) and leveraged it to design a robust controller to track a reference lift profile with H_∞ loop-shaping approach. However, the use of classical aerodynamic models relies strictly on the fully attached flow assumption, and linear descriptions of the aerodynamics tend to fail if flow separation is induced, as is prone to occur when the disturbance is of large amplitude. In such circumstances one can no longer rely on superposition of indicial disturbance responses from sequences of gusts. Linear control tends to show degraded performance or even fail in these strong-gust conditions. In the absence of linear superposition, the control task is further confounded by the vast parameter space of the gusts and the strong nonlinear interactions with the wings (Jones 2020; Jones *et al.* 2022).

Therefore, this challenge has spurred a large number of studies on modeling the nonlinear flow response and designing the appropriate control strategies when the flow is not fully attached. One popular approach is to linearize the flow around an equilibrium condition (Rowley 2005; Ma *et al.* 2011; Brunton *et al.* 2013). However, the limitation of this approach is that the model would be accurate only when the flow condition is near the equilibrium condition. Therefore, a gain-scheduling approach can be used to construct a series of linear models based on a series of equilibrium points. For example, Dawson *et al.* (2015) constructed 8 linear models for each corresponding to an incremental range of angle of attack, and these models could be switched during random pitch motion. However, they found that switching between the models leads to some degradation of accuracy when the pitching rate becomes relatively large. To address this problem, some other approaches have been pursued that incorporate proxy parameters of the relevant fluid flow physics into the system equations, such as linear parameter-varying model (Hemati *et al.* 2017), Goman-Khrabrov model (Goman & Khrabrov 1994; Williams & King 2018), and the time delay and decay model (An *et al.* 2016). Although these models show improved performance, their effectiveness depends heavily on the appropriate selection and fine-tuning of proxy parameters, which raises concerns about their generalizability in the vast parameter space of gust disturbances (Jones 2020) and the diversity of available actuation mechanisms. Therefore, the development of a more generalizable and adaptive control strategy is still an open and compelling challenge.

Fortunately, the development of machine learning and data science potentially provides us with data-driven tools to better model and control these complex flow problems. Among them, reinforcement learning (RL)—particularly when outfitted with a deep network for nonlinear function approximation, commonly referred to as deep reinforcement learning—has demonstrated notable success in a variety of flow control tasks. The examples include exploring effective swimming strategies (Novati *et al.* 2017; Verma *et al.* 2018), learning an optimized foil flapping motion (Wang *et al.* 2024), reducing drag of a bluff body (Fan *et al.* 2020; Rabault *et al.* 2019; Xia *et al.* 2024), mitigating lift variation of an airfoil (Liu *et al.*

2025; Beckers & Eldredge 2024; Renn & Gharib 2022), laminarizing a turbulent Couette flow (Linot *et al.* 2023), and many others.

Despite these advances, identifying an effective control strategy by RL still remains challenging in real aerodynamic flows, where a sequence of gusts, such as those caused by atmospheric variations or wake interactions, can impose a succession of large-amplitude time-varying disturbances to the flow. There are a few pressing questions that underlie this problem. The first two pertain to reducing the number of costly trial-and-error interactions with the environment required for training. First, can we improve the training process by building from our prior expertise in linear control rather than from scratch? Second, given the infinite variety of possible gusts, either single or in sequences, what is a sufficient training regimen for learning a generally effective control strategy? We propose some approaches to addressing these questions below.

The third question stems from the fact that, from a practical (i.e., limited) number of sensors, fluid flows are only partially observable. How can we parse the available information in these sensors to ascertain the state of the flow for choosing an appropriate control action? As in previous studies of RL control in fluid dynamics (Beckers & Eldredge 2024; Xia *et al.* 2024; Wang *et al.* 2024; Weissenbacher *et al.* 2025), we address this question by exploiting information in extended time records of the sensor measurements. The implicit objective of this approach is to infer a disturbance through the temporal signature it leaves in the sensors. For this task, we follow an approach similar to one recently used by Wang *et al.* (2024) and make use of the machine learning concept of *self-attention*. A transformer (Vaswani *et al.* 2017), the simplest and most widely-used machine learning architecture that exploits this concept, identifies correlations between different (and possibly widely separated) parts of the input observation sequence to approximate an output. We use the transformer output to approximate a belief state, which is used in turn to choose a corresponding control action via the proximal policy optimization (PPO) algorithm (Schulman *et al.* 2017).

In the present study, we demonstrate the training and use of our transformer-based RL framework on gust encounters in a CFD-based flow environment. Sparse pressure measurements on the surface of a two-dimensional flat plate are used to detect disturbances and the lift is regulated via pitch control. We learn mid-chord and quarter-chord pitching control strategies in both single- and multiple-gust environments, and show that the policy obtained from the multiple-gust training is sufficient for controlling arbitrarily-long gust sequences. To accelerate training, we adopt a pretraining approach that leverages expert data from a well-designed proportional control (P control) strategy. We demonstrate that this warm-start technique significantly speeds up convergence compared to training from scratch. Performance comparisons show that the RL control strategy outperforms the P-control baseline, with an increasingly pronounced advantage as the number of gusts grows, in both pivot configurations. Furthermore, we show that the quarter-chord pitching strategy spends much less control effort while achieving the lift regulation better than in mid-chord pitching. By analyzing the vorticity field, pressure distribution, lift history, and the corresponding pitching history of the flat plate, we offer physical insights into the superiority of quarter-chord pitching control. Finally, we investigate the generalizability of the trained RL agent via transfer learning in a multiple-gust environment with a quarter-chord pitching configuration.

The remainder of the paper is organized as follows. The set-up and description of the flow control problem, and the details about the transformer-based RL framework, are discussed in §2. Then, we analyze the performance of the RL control strategy across different scenarios and pivot locations, accompanied by a discussion of the underlying physical mechanisms, in §3. Finally, we summarize and discuss the results in §4.

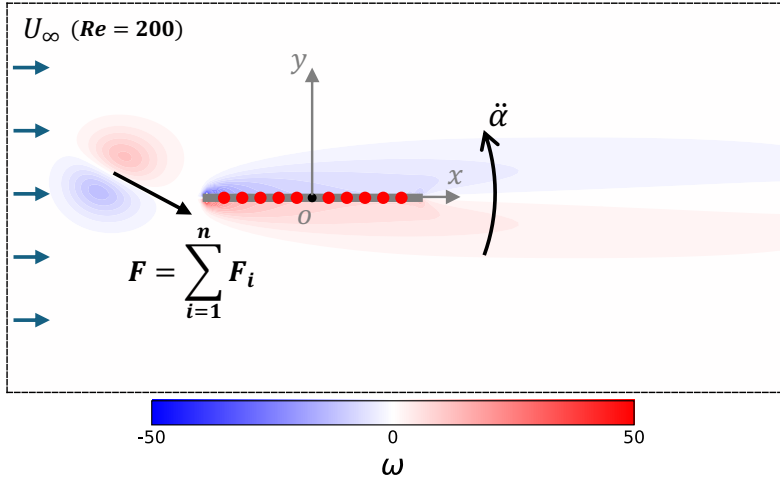


Figure 1: Control problem description. We only show the pivot point located at the mid chord for simplicity, shown as grey dot, but a quarter chord pivot point configuration is also investigated in this study. The pressure sensors are denoted as the red dots. The colorbar shown here is used throughout this study.

2. Methodology

2.1. Flow control problem description

In this study, we investigate a control strategy for regulating the lift of a flat plate of chord length c in a two-dimensional flow with $Re = \rho U_\infty c / \mu = 200$, where U_∞ is the freestream velocity and ρ and μ are the density and dynamic viscosity of the fluid, respectively. Specifically, the objective of the lift regulation in this study is to track a reference lift of zero during gust encounters by pitching the plate about a pivot axis. However, the proposed methodology is general and, within physical limits, can be easily extended to track arbitrary reference lift profiles with other actuation methods. As depicted in figure 1, gusts are introduced in the region upstream of the plate after the undisturbed flow is fully developed. For reference, the coordinate system is centered at the mid chord point of the plate when the plate is at zero pitch angle, with x in the freestream direction.

Specifically, gusts are introduced successively, with each gust i generated via a body force applied on the fluid, Gaussian-distributed in both space and time according to

$$F_i(x, y, t) = \rho U_\infty c^2 \frac{(D_x, D_y)}{\pi^{3/2} \sigma_x \sigma_y \sigma_t} \exp \left[-\frac{(x - x_0)^2}{\sigma_x^2} - \frac{(y - y_0)^2}{\sigma_y^2} - \frac{(t - t_0)^2}{\sigma_t^2} \right], \quad (2.1)$$

where D_x and D_y denote the dimensionless amplitudes of the Gaussian forcing in the respective coordinate directions, and σ_x , σ_y specify the respective spatial spreads in these directions. The spatial center of the forcing is described by x_0 and y_0 , while t_0 and σ_t represent the temporal center and spread, respectively. The forcing field acts as a source term in the Navier–Stokes equations and thus generates a distributed region of vorticity in the fluid that subsequently convects and diffuses with the flow. The Gaussian spatial and temporal distributions ensure that this new vorticity comes in the form of vortices that are localized (but continuous) in space and time. This approach enables us to introduce gusts continuously, rather than creating them impulsively at a single instant, e.g., through initial conditions.

For training and testing purposes, several of the gust parameters in (2.1) vary from case to case, and, in the case of successive gusts, from gust to gust. The parameter space of

	D_x	D_y	x_0/c	y_0/c	$\sigma/c = \sigma_x/c = \sigma_y/c$	$U_\infty t_0/c$	$U_\infty \sigma_1/c$
1st gust	1.2	[-1, 1]	-1.0	[-0.25, 0.25]	[0.05, 0.1]	0.5	0.2
2nd gust	1.2	[-1, 1]	-1.0	[-0.25, 0.25]	[0.05, 0.1]	{0.9, 0.95, 1.0, 1.05, 1.1}	0.2
3rd gust	1.2	[-1, 1]	-1.0	[-0.25, 0.25]	[0.05, 0.1]	{1.4, 1.45, 1.5, 1.55, 1.6}	0.2
...					...		
8th gust	1.2	[-1, 1]	-1.0	[-0.25, 0.25]	[0.05, 0.1]	{3.9, 3.95, 4.0, 4.05, 4.1}	0.2

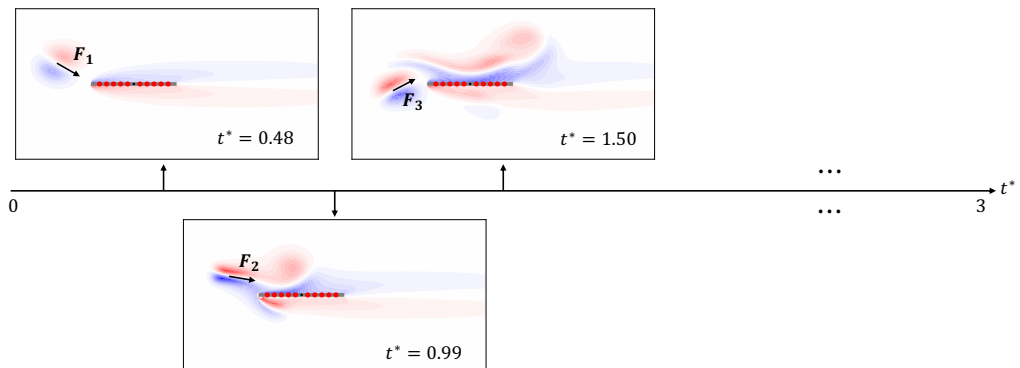
Table 1: Parameter space of n -successive gusts in this study.

Figure 2: An example of environment with three successive gust under no control. t^* is the convective time. The specific gust parameters, for this example, by the order of $(D_y, y_0/c, \sigma/c, U_\infty t_0/c)$ is: $(-1.0, 0.25, 0.1, 0.5)$, $(-0.5, 0.25, 0.05, 1.0)$, $(1.0, -0.1, 0.075, 1.5)$.

n -successive gusts (up to the maximum used in this study, eight) is given in table 1. Some parameters remain fixed, others are chosen from a continuous range, and the temporal center of each gust is selected from a discrete set. The purpose of the time gap between the temporal centers of successive gusts is to simulate sequential gust encounters, as commonly observed in real disturbed flow environments such as wake regions. An example with three successive gusts is shown in figure 2 to illustrate how n -successive gusts are implemented in this study.

The control input in this study is the angular acceleration $\ddot{\alpha}$ of the plate about a fixed pivot point, located at either mid chord or quarter chord. In order to simulate a practical control problem with limited bandwidth, we restrict the angular acceleration $\ddot{\alpha}$ to be piecewise constant over each control step, Δt_c^* (taken to be five time steps of the flow solver $\Delta t_c^* = 5\Delta t^*$), and confined to a range $\ddot{\alpha} c^2/U_\infty^2 \in [-10, 10]$. This range is not based on a specific actuator but it serves to reflect a general physical limitation on actuation in a practical system and to ensure numerical stability during the learning process. Measurements from the system comprise the pressure jump coefficients

$$C_{\Delta p}^j = \frac{P_l^j - P_u^j}{\frac{1}{2}\rho U_\infty^2}, \quad j = 1, 2, \dots, 10, \quad (2.2)$$

obtained from 10 pressure sensors symmetrically distributed on the surface of the flat plate—five placed uniformly between the mid-chord and the edge on each half of the plate—where P_l^j and P_u^j are the surface pressures on the lower and upper sides, respectively; the lift

coefficient

$$C_L = \frac{F_y}{\frac{1}{2}\rho U_\infty^2 c}, \quad (2.3)$$

where F_y is the y component of the force exerted on the flat plate by the surrounding fluid; and the pitching angle α , defined as the angle between the chord axis and x axis and defined to be positive in the counter-clockwise direction. Before gusts are introduced, the flat plate has an initial pitching angle $\alpha = 0$ and an initial angular velocity $\dot{\alpha} = 0$.

The flow environment is simulated computationally with a viscous incompressible flow solver based on the immersed boundary projection method (Eldredge 2022). The flow solver employs a vorticity-streamfunction formulation and utilizes a lattice Green’s function to solve the streamfunction Poisson equation, allowing for a more compact domain compared to traditional computational aerodynamics studies. From here on, we only report the time in convective time units, $t^* = tU_\infty/c$, and the spatial coordinates in chord lengths, $x^* = x/c$ and $y^* = y/c$. The computational domain spans $[-1.395, 2.175]$ in the x^* direction and $[-0.885, 0.885]$ in the y^* direction and employs free-space conditions on all boundaries. In this computational domain setup, the vortex gust and the resulting airfoil response are ensured to remain between the upper and lower boundaries and freely convect through the downstream boundary. We employ a uniform Cartesian grid with grid size $\Delta x^* = 0.015$ and a uniform time step size $\Delta t^* = 0.006$. Each simulation case lasts for 3 convective time units, but is truncated early if $|\alpha| > \pi/4$ to avoid unrealistic configurations.

2.2. Reinforcement learning framework

In this section, we describe how the flow control problem is formulated into a reinforcement learning (RL) framework. As figure 3 shows, the basic RL framework, consisting of the environment and agent, is expressed as a Markov decision process (MDP). A MDP models the decision-making process by a tuple $\{\mathcal{S}, \mathcal{A}, \mathcal{T}, \mathcal{R}, \gamma\}$ where \mathcal{S} is the state space, \mathcal{A} is the action space, \mathcal{T} is the transition probability function, \mathcal{R} is the reward function, and γ is the discounted factor: the agent receives a full state $s \in \mathcal{S}$ and selects an action $a \in \mathcal{A}$, the state s is transitioned to a new state s' according to the transition probability function $\mathcal{T}(s'|s, a)$, and a reward is also generated from $r = \mathcal{R}(s, a)$. However, the full state s is not accessible in many real world systems, particularly in fluid dynamics, where this state includes the entire flow field. Instead, we only have partial information about the full state s from available sensors, which leads to its formulation as a partial observable Markov decision process (POMDP) (Åström 1965; Kaelbling *et al.* 1998). A POMDP extends the MDP tuple to $\{\mathcal{S}, \mathcal{A}, \mathcal{O}, \mathcal{T}, \mathcal{Z}, \mathcal{R}, \gamma\}$ where, in addition to the MDP components, \mathcal{O} is the observation space and $\mathcal{Z} = \mathcal{Z}(o'|s, a)$ is the observation function, representing the probability of receiving observation o' given the state s and action a . Therefore, instead of making a decision based on full state s as in a MDP, the agent in a POMDP makes a decision based on a belief state $b(s)$, which represents a probability distribution over all possible states given the agent’s observation history. The agent learns a policy $\pi = \pi(a|b(s))$ —that is, a policy conditioned on the distribution of possible states—that maximizes the discounted return

$$J(\pi) = \mathbb{E} \left[\sum_{t=0}^{\infty} \gamma^t r_t \mid \pi \right]. \quad (2.4)$$

As we discussed above, the agent relies on a belief state $b(s)$ to make a decision in a POMDP, which requires past observed information. Some RL algorithms propagate this belief state forward in time by folding in observations, and then condition their actions based on the most probable state. This approach is challenging in a fluid dynamics environment,

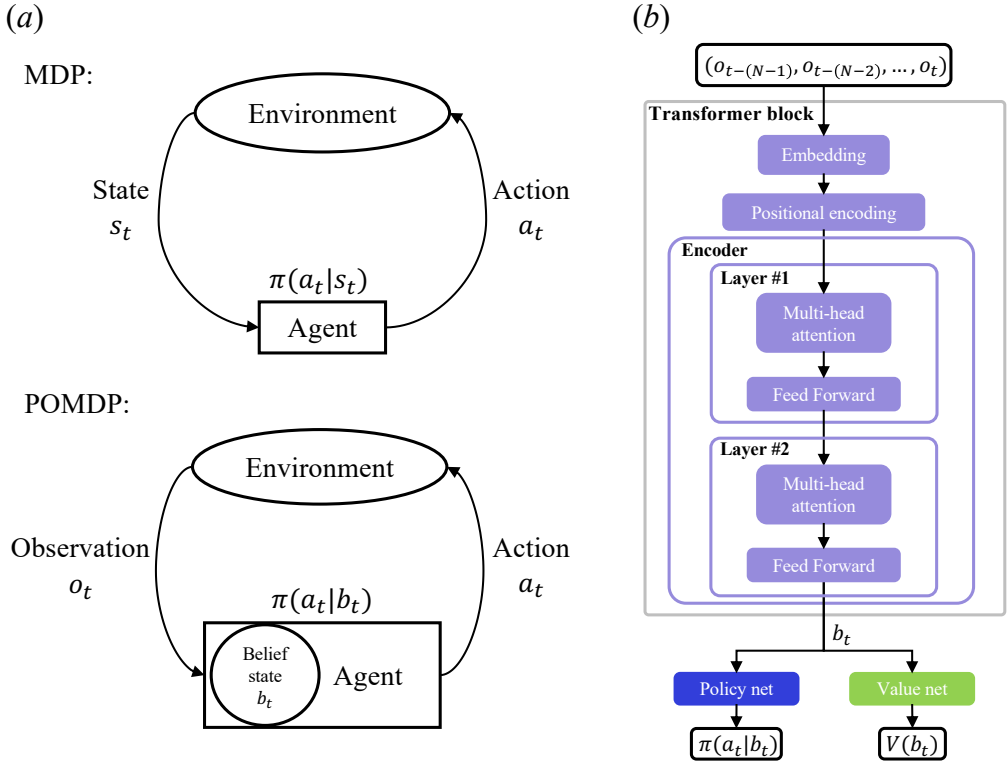


Figure 3: (a) Comparison between MDP and POMDP. (b) The schematic figure of transformer and the subsequent policy and value networks.

where the state is high dimensional, though there has been recent success in sequentially estimating lower-dimensional representations of the flow state (Mousavi & Eldredge 2025). Alternatively, in fluid dynamics, some studies have directly employed the past observation history as a reduced representation of the state to approximate a POMDP as a MDP (Beckers & Eldredge 2024; Xia *et al.* 2024; Weissenbacher *et al.* 2025). Francois-Lavet *et al.* (2019) have shown that the agent can learn to encode the relevant past observations into a latent representation that serves as a surrogate of the probable state and make a decision based on this latent representation. Therefore, sequence models, such as recurrent neural networks (RNNs) (Rumelhart *et al.* 1986) and transformers (Vaswani *et al.* 2017), play an important role since they can extract meaningful information from a time-dependent history sequence. One form of RNN, the long-short term memory (LSTM) (Hochreiter & Schmidhuber 1997), has been successfully applied to many complex fluid systems to model time-dependent behavior (Liu *et al.* 2025; Hou *et al.* 2019; Hasegawa *et al.* 2020). The mechanism of the LSTM is to update a hidden state at each time step based on the previous hidden state information and the new observation. This approach has two limitations: it is difficult to retain the information from distinct past observations when the sequence is very long, and the recursive process makes it impossible to process the sequence in parallel.

The limitations of the RNN motivate the recent popularity of the transformer (Vaswani *et al.* 2017), which leverages the self-attention mechanism to model a time sequence simultaneously. Specifically, the transformer first embeds the observation sequence into a higher dimensional space of tokens using a linear projection and a positional encoding (to

ensure that temporal information is included):

$$f(o_{t-(N-1)}, o_{t-(N-2)}, \dots, o_t) = (x_{t-(N-1)}, x_{t-(N-2)}, \dots, x_t), \quad (2.5)$$

where $o_t \in \mathbb{R}^{d_{\text{obs}}}$ is the observation at time step t , $x_t \in \mathbb{R}^{d_{\text{model}}}$ is the embedded token at the corresponding time step, and N is the observation window size, i.e., the observation sequence length. After embedding the observation sequence, the transformer applies the multi-head self-attention mechanism, wherein each embedded token dynamically attends to all N tokens in the sequence by computing the query \mathbf{Q} , the key \mathbf{K} , and the value \mathbf{V} for each attention head. Each attention head $m = 1, \dots, n_{\text{head}}$ uses separate learnable matrices $\mathbf{W}_{\mathbf{Q}}^{(m)}, \mathbf{W}_{\mathbf{K}}^{(m)}, \mathbf{W}_{\mathbf{V}}^{(m)} \in \mathbb{R}^{d_{\text{model}} \times d_k}$, where $d_k = d_{\text{model}}/n_{\text{head}}$, to compute

$$\mathbf{Q}^{(m)} = \mathbf{X}\mathbf{W}_{\mathbf{Q}}^{(m)}, \quad \mathbf{K}^{(m)} = \mathbf{X}\mathbf{W}_{\mathbf{K}}^{(m)}, \quad \mathbf{V}^{(m)} = \mathbf{X}\mathbf{W}_{\mathbf{V}}^{(m)}, \quad (2.6)$$

where $\mathbf{X} = [x_{t-(N-1)} \ x_{t-(N-2)} \ \dots \ x_t]^T \in \mathbb{R}^{N \times d_{\text{model}}}$ is a matrix whose rows comprise the N embedded tokens of the input sequence. The i th row of $\mathbf{Q}^{(m)}$, the query vector $Q_i^{(m)} \in \mathbb{R}^{d_k}$, represents what the i th token is looking for from the other tokens. The i th row of $\mathbf{K}^{(m)}$, the key vector $K_i^{(m)} \in \mathbb{R}^{d_k}$, represents the features of the i th token that provide for other tokens to attend to. The i th row of $\mathbf{V}^{(m)}$, the value vector $V_i^{(m)} \in \mathbb{R}^{d_k}$, is the actual information carried by the i th token. For each attention head, the scalar-valued attention score $\alpha_{ij}^{(m)}$ between the i th and j th tokens is computed by

$$\alpha_{ij}^{(m)} = \frac{Q_i^{(m)} \cdot K_j^{(m)}}{\sqrt{d_k}}, \quad (2.7)$$

representing how much attention the i th token should pay attention to the j th token. This attention is used to assemble the output $h_i^{(m)} \in \mathbb{R}^{d_k}$ as the weighted sum of the value vectors $V_j^{(m)}$,

$$h_i^{(m)} = \sum_{j=1}^N \text{softmax}(\alpha_{ij}^{(m)}) V_j^{(m)}. \quad (2.8)$$

The final output $h_i \in \mathbb{R}^{d_{\text{model}}}$ is obtained by concatenating the $h_i^{(m)}$ from each head into a single vector:

$$h_i = \text{Concat} \left(h_i^{(1)}, \dots, h_i^{(n_{\text{head}})} \right), \quad (2.9)$$

and represents the contextualized representation of the i th token. This output of the self-attention layer is fed into the feedforward network layer, which introduces nonlinearity to refine the token representation. The combination of the self-attention layer and the feedforward layer is an encoder layer. In the current work, our transformer employs two encoder layers with two attention heads in each layer. After the observation sequence $(o_{t-(N-1)}, o_{t-(N-2)}, \dots, o_t)$ is processed by the two-layer transformer structure, we obtain a sequence of contextualized representations $(\tilde{h}_{t-(N-1)}, \tilde{h}_{t-(N-2)}, \dots, \tilde{h}_t)$, where $\tilde{h}_t \in \mathbb{R}^{d_{\text{model}}}$ incorporates information from the entire observation window. In the current work, we extract the final element \tilde{h}_t from this sequence and treat it as the latent representation of the probable state. This latent representation is then passed to the policy and value networks, which provide the probability distribution over the action space (for action selection) and the approximated expected return on that state (for state-value estimation), respectively. Figure 3(b) summarizes this framework. For clarity, $d_{\text{obs}} = 12$, $d_{\text{model}} = 32$, $d_k = 16$, and $n_{\text{head}} = 2$ in this study.

We use the proximal policy optimization (PPO) algorithm (Schulman *et al.* 2017) to approximate the optimal policy. Both the policy and the value networks consist of two hidden layers with 32 hidden units each, where each hidden layer employs a Rectified Linear Unit activation function. The loss function that training seeks to minimize comprises three components. PPO, as a gradient-based model-free algorithm following the actor-critic framework, introduces a clipped surrogate objective to ensure updating within a safe region, constituting the first loss component

$$L_{\theta}^{\text{policy}} = \mathbb{E}_t [\min(\rho_t A_t, \text{clip}(1, 1 - \epsilon, 1 + \epsilon)A_t)], \quad (2.10)$$

where $\rho_t = \pi_{\theta}(a_t|s_t)/\pi_{\theta_{\text{old}}}(a_t|s_t)$ is the ratio of updated and old policies; A_t is the advantage function, which helps the agent evaluate how good the action a_t is at state s_t compared to the expected value of this state $V(s_t)$; and ϵ is the clip hyperparameter that controls the size of the safe region. The advantage function is estimated from the generalized advantage estimation (GAE) (Schulman *et al.* 2018), defined as

$$A_t^{\text{GAE}} = \sum_{l=0}^{\infty} (\gamma\lambda)^l \delta_{t+l}, \quad (2.11)$$

where $\delta_t = r_t + \gamma(1 - d_t)V_{\phi}(s_{t+1}) - V_{\phi}(s_t)$ is the temporal difference residual, and λ is a hyperparameter that controls the trade-off between the variance and bias of the estimator. The variable $d_t \in \{0, 1\}$ is a Boolean terminal signal indicating whether the next state s_{t+1} is terminal (i.e., $d_t = 1$) or not (i.e., $d_t = 0$). Furthermore, the value loss function is defined as

$$L_{\phi}^{\text{value}} = \mathbb{E}_t \left[(r_t + \gamma V_{\phi}(s_{t+1}) - V_{\phi}(s_t))^2 \right], \quad (2.12)$$

where γ is the discounted factor. For encouraging exploration, an entropy loss is incorporated

$$L^{\text{entropy}} = \mathbb{E}_t \left[- \sum_{a_t} \pi(a_t|s_t) \log \pi(a_t|s_t) \right]. \quad (2.13)$$

Finally, we formulate the total loss as

$$L(\theta, \phi) = L_{\theta}^{\text{policy}} + C_V L_{\phi}^{\text{value}} - C_E L^{\text{entropy}}, \quad (2.14)$$

where C_V is the value coefficient and C_E is the entropy coefficient.

RL training requires a large number of interactions between the agent and the environment (in this paper, CFD) if it starts from scratch, and thus the application of RL may be impeded in expensive environments (e.g., flow control around a three-dimensional wing shape). Therefore, in some problems in this paper we will seek to accelerate training by using a pretraining technique to initialize a structured policy from expert data, i.e., actions obtained from a prior control strategy that performs reasonably well. In the present work, this prior strategy is P control, and the pretrained policy is derived by sampling actions on trajectories that follow the proportional control strategy. Specifically, we find an initial policy that minimizes a loss function as follows:

$$L_{\theta}^{\text{pretraining}} = \mathbb{E}_{\mathcal{D}} [a_{\text{expert}} - \hat{a}], \quad (2.15)$$

where a_{expert} is the expert action, i.e., the target, collected from the sampled expert trajectories \mathcal{D} , and \hat{a} is the output from the transformer policy network.

We summarize the overall transformer-based RL framework in Figure 4. From the initial policy network, which may be random or initialized by pretraining, we move on to the RL training. A parallel environment is employed to enhance the data efficiency. As described

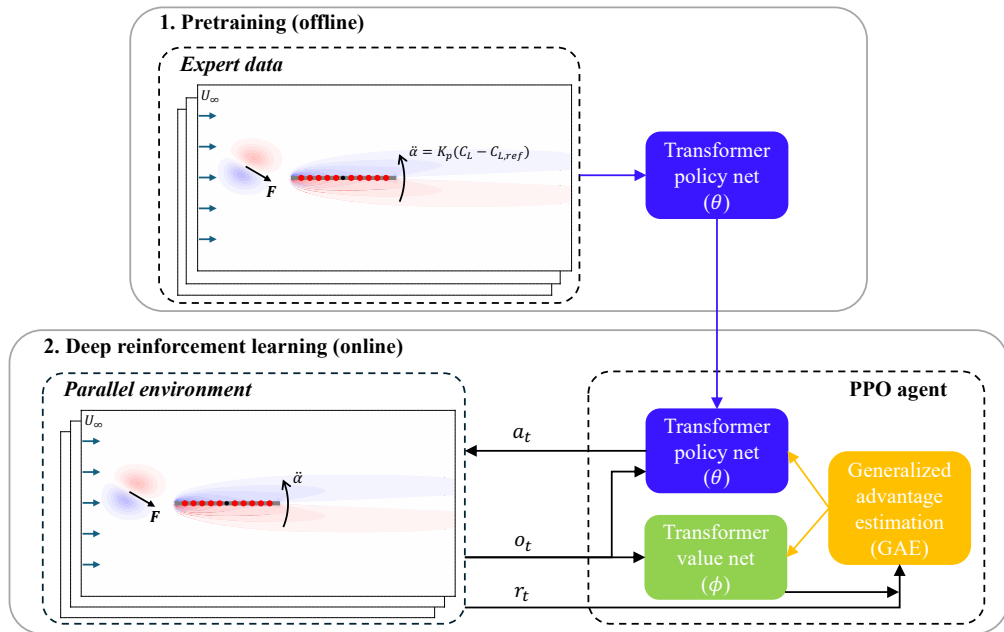


Figure 4: Overview of the transformer-based RL framework

above, the action a_t in this paper is defined as the angular acceleration $\ddot{\alpha}$ about a fixed pivot point and the observation o_t is defined as a vector consisting of 10 pressure sensor measurements over the surface of the flat plate with the locations indicated by the red dot in figure 4, the lift coefficient, and the pitching angle:

$$o_t = \left[C_{\Delta p}^1 \cdots C_{\Delta p}^{10} C_L \alpha \right]_t. \quad (2.16)$$

From previous work (Mousavi & Eldredge 2025), it has been shown that surface pressure can be informed effectively by the change of flow field, and thus we incorporate surface pressure into the observation function. An observation window with a size of $N = 20$ is employed throughout this study. Since we aim to find an optimal policy that enables the agent to track a reference lift profile, we design the reward function as follows:

$$r_t = 1 - \left(\frac{C_{L_t} - C_{L_{\text{ref}}}}{C_{L_{\text{scale}}}} \right)^2 - \left| \frac{\ddot{\alpha}_t - \ddot{\alpha}_{t-1}}{\ddot{\alpha}_{\text{scale}}} \right| - \begin{cases} 100, & \text{if truncated,} \\ 0, & \text{otherwise.} \end{cases} \quad (2.17)$$

The first term serves as a baseline reward at each time step, ensuring that the maximum reward under an ideal control strategy is 1, facilitating stable learning. The second term in (2.17) penalizes the deviation of the lift coefficient C_L from the reference lift $C_{L_{\text{ref}}}$, with the denominator $C_{L_{\text{scale}}}$ included to scale this term to an appropriate weight in the overall reward; a quadratic form is chosen to amplify large deviation compared to a linear penalty, and this choice is confirmed from empirical observations that it significantly improves the learning performance, likely due to a smoother gradient behavior during the policy optimization. The third term penalizes temporal changes of the control input, encouraging a smoother control process and avoiding an unrealistically aggressive actuation; the scale factor $\ddot{\alpha}_{\text{scale}}$ modifies its relative importance in the total reward. The final term imposes a large penalty on episodes that truncate prematurely due to exceeding the feasible range of pitching angle, i.e.

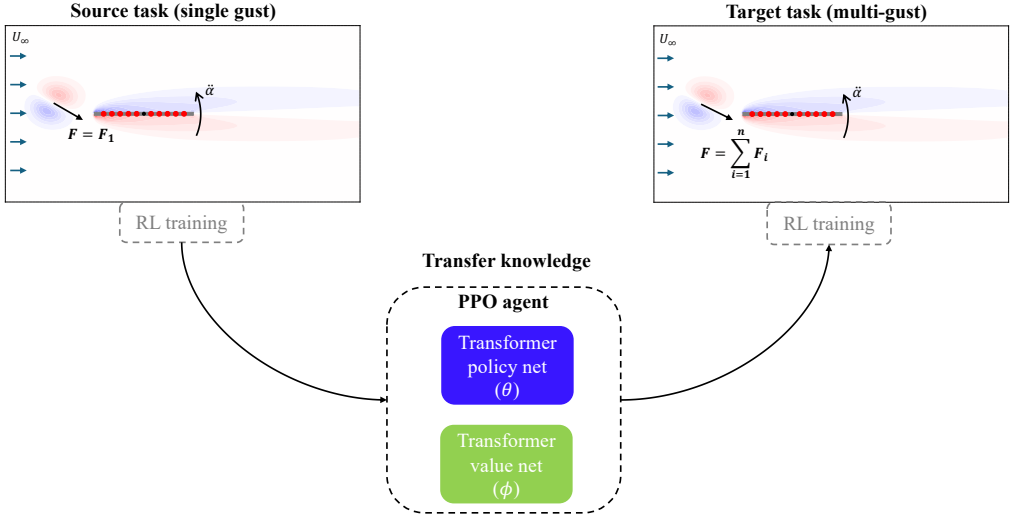


Figure 5: Overview of the transfer learning.

$|\alpha| > \pi/4$. The reference lift in this study is set to zero, $C_{L_{ref}} = 0$, and based on experience, we set $C_{L_{scale}} = 0.3$ and $\ddot{\alpha}_{scale} = 10$ throughout the study.

Before we complete this description of the methodology, we described one more technique that we use in this paper to accelerate the training. Finding a good expert policy from which to initiate training is often nontrivial. Therefore, we also propose a strategy of transfer learning (Bozinovski 2020). As depicted in Figure 5, the RL agent is first trained in a single-gust environment (the source task), and once it acquires sufficient knowledge, the learned policy and value networks are transferred to a multi-gust environment (the target task), thereby accelerating learning and reducing training cost. This approach facilitates the application of RL to environments in which training is more expensive: by first training a RL agent in a relatively easy or simplified environment, we obtain a well-informed initialization that serves as a warm start in the subsequent RL training in a more complex environment, and thus the overall training cost may be reduced.

3. Results and discussion

In this section, we demonstrate the training, performance, and generalizability of the proposed transformer-based RL framework on the lift regulation problem. The first part of the study, in §3.1 and §3.2, utilizes the mid-chord pitching configuration. In §3.1 we benchmark the performance of P control and RL control in a baseline environment, comprising a single gust. We then investigate the generalizability of the RL design approach in §3.2 by extending to an environment that includes multiple gusts. Then, we focus attention on the quarter-chord pitching configuration in §3.3 and §3.4. We first study the effect of this change of pivot point location in the single-gust environment in §3.3, devoting particular attention to the physics of the two different configurations. Finally, we investigate the extension of the RL control strategy to a multi-gust environment by transfer learning in §3.4. For reproducibility, the essential hyper-parameters for all configurations and gust environments are summarized in table 2.

	learning rate	clipping ratio	value coefficient	entropy coefficient	number of parallel envs.	inner epochs	discount factor	GAE lambda	gradient clipping
scratch (single)	0.0001	0.2	0.5	0.005	24	24	0.99	0.95	0.5
pretrain (single)	0.0001	0.1	0.5	0.005	24	8	0.99	0.95	0.5
scratch (multiple)	0.0001	0.2	0.5	0.005	72	72	0.99	0.95	0.5
pretrain (multiple)	0.0001	0.1	0.5	0.005	72	8	0.99	0.95	0.5

Table 2: Summary of the essential hyper-parameters for all different configurations.

3.1. Benchmarking control performance: mid-chord pitching in single-gust environment

We begin by investigating a baseline environment, which is characterized by a single upstream gust. This configuration is set up to be a benchmark for comparing the performance of P control against RL control. Specifically, we intend to evaluate how well each approach can mitigate the lift variation induced by the gust, and to establish a performance baseline before we move on to a more complex environment. The P control strategy, also explored in previous work as a baseline for RL (Beckers & Eldredge 2024), is defined as follows:

$$\ddot{\alpha} = K_p(C_L - C_{L_{\text{ref}}}), \quad (3.1)$$

where K_p is the proportional control gain to be determined. Rather than train a RL agent from scratch, which requires a significant number of interactions, we hypothesize that we can leverage a P control strategy with a good K_p value to pretrain the RL agent and continue the subsequent RL training from this warm start in order to make the learning process converge faster.

We show the learning envelope for the RL agents starting from scratch and those pretrained with P control in figure 6. We report the total reward $\sum r_t$ in each episode as the criterion to evaluate the performance of the RL agent evolves with the number of training episodes. We can first observe that the red learning envelope, which corresponds to learning from scratch, starts with an episode reward of approximately -430 , reflecting the poor performance of an uninformed random policy. An episode total reward of 0 is not reached until around the 300th episode, there is substantial variance throughout the learning process, and the learning envelope is still not fully converged until the 600th episode. This behavior reflects the high cost of exploration typically required for the agent to discover a viable control strategy. In contrast, when we start with a well-informed pretrained policy, as in both the orange and green learning envelopes, we have a much higher initial episode total reward and the training curve exhibits significantly less variance. This highlights the benefit of pretraining in enabling the agent to avoid extensive and inefficient exploration. Among the two pretrained strategies, a pretrained policy obtained from a P control strategy with $K_p = 80$ (in green) has a higher initial total reward than the one that is pretrained with $K_p = 10$ (in orange), and thus, the former is already converged at the 100th episode, whereas the latter is still converging, though likely to finish in modestly more episodes. Therefore, these results show that strong expert data for pretraining helps the RL agent converge faster.

For further evaluation we focus on the fully-trained RL agent initialized from a pretrained P control policy with $K_p = 80$. To assess the policy’s robustness, RL agents are picked from the last five episodes. In figure 7 we compare these agents with control strategies

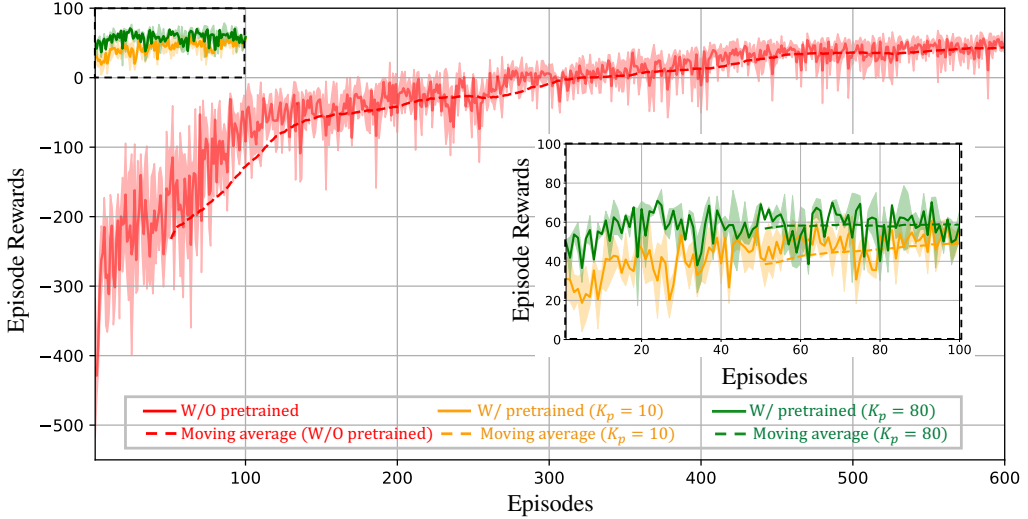


Figure 6: Learning envelopes for mid-chord pitching RL agents in single-gust environment. The solid lines and the shadow regions are the mean and standard deviation across three different runs. The dashed lines show the moving average with an averaging window of 50 episodes. The inset plot is a zoomed-in view for the learning envelopes of RL agents starting from pretrained models. At each episode index, the episode reward is averaged across all parallel environments per run.

based only on P control. It should be noted that, although the P control only penalizes the instantaneous lift error ($C_L - C_{L_{ref}}$), we evaluate its performance using the same reward function employed during the RL training. This reward function is a more comprehensive and practical evaluation metric, incorporating the lift track error but also penalizing aggressive control input and unrealistic configurations, thereby balancing the precision with smoothness and stability. Thus, we acknowledge that there is a slight mismatch in the evaluation basis. Later in this section, we will compare the different control strategies in individual episodes on the basis of lift variation alone.

From figure 7, we can observe that starting from $K_p = 0$, i.e. no control, the performance of the P control improves with increasing gain until $K_p = 60$, where it shows the optimal performance of all the P control strategies. Beyond that value of K_p , the P control starts to deteriorate, particularly after $K_p = 100$, indicating that an excessively high gain causes instability and an overreaction to the gust disturbances. We can observe that the envelope of trained RL control strategies (shown as a blue envelope) improve upon the performance of the initial pretrained policy (shown as a blue dashed line) and outperform the best P control across the tested K_p region. However, the performance gap between the mean of RL control and the best P control is only approximately 0.4, showing that linear control is an effective control strategy for single-gust episodes mitigated by mid-chord pitching and RL does little to improve on it. We expect this performance gap will become larger as the number of gusts increases which would introduce higher nonlinearity, as we will discuss in §3.2.

To demonstrate the performance of the different control strategies, we show the corresponding lift profile and the action profiles for two representative cases in figure 8. For each representative case, we also report the corresponding L_2 norm of the lift coefficient history $\|C_L\|_2$ (to measure the lift tracking error) and the action history $\|\ddot{\alpha}\|_2$ (to quantify the total control effort), as well as the episode reward $\sum r_t$. For clarity, the P control here corresponds to $K_p = 60$ due to its optimal performance in figure 7. For both representative cases, we observe that RL control shows an almost identical lift tracking error to the best P control, but

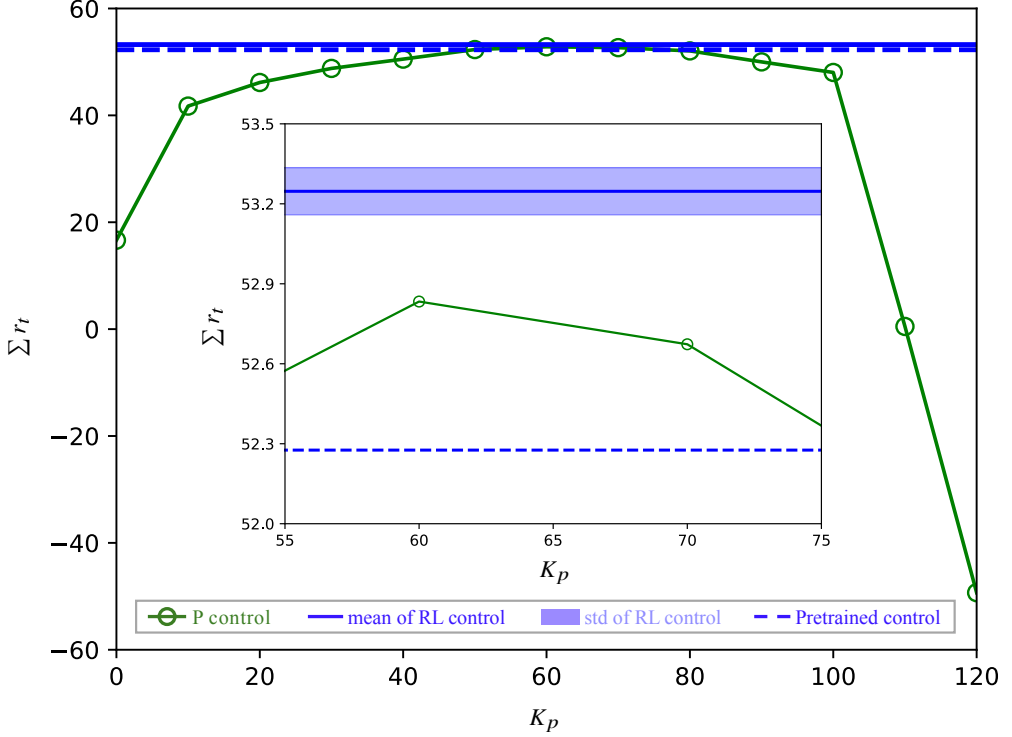


Figure 7: Evaluation of proportional control and RL control in single-gust environment. The statistics for each data point is averaged over 15 random cases. The blue solid line and shadow region represent the mean and standard deviation value for the RL agents in the last 5 episodes. The dashed line represents the pretrained RL agent. The inset figure is a zoom-in view for K_p from 55 to 75.

requires a smaller control effort, and thus the episode reward of the RL control is slightly higher than the best P control. This performance difference is also apparent in the profiles. Specifically, the RL control returns a C_L history that is almost indistinguishable from the best P control, but the $\ddot{\alpha}$ histories behave visibly differently. For example, we can see from the representative case 1 that the RL control learns to smooth out the small temporal fluctuation of $\ddot{\alpha}$ at around 0.75 convective time. The results of the two representative cases suggest that a well-tuned P control can perform effectively in this relatively simple configuration. In this sense, the RL agents act as a fine-tuned version of the P controller, optimizing the performance in a nuanced manner.

By comparing the two representative cases, we also see that the C_L profile under RL control still shows a small bump in representative case 1, whereas it is not present in representative case 2. This discrepancy can be attributed to the magnitude constraint we impose on the angular acceleration $\ddot{\alpha}$. This is clear from the $\ddot{\alpha}$ history, in which we can see that the time corresponding to the small bump in representative case 1 coincides with the time at which the $\ddot{\alpha}$ reaches the magnitude constraint and also with the interval that the gust induces a huge lift variation on the plate without control. In contrast, in representative case 2, the $\ddot{\alpha}$ history remains well within the bound, and the lift variation without control remains relatively moderate throughout the episode. As a result, the corresponding C_L history under RL control tracks the zero reference lift very accurately. This observation highlights that the actuation limit can restrict the performance of the controller to fully compensate for

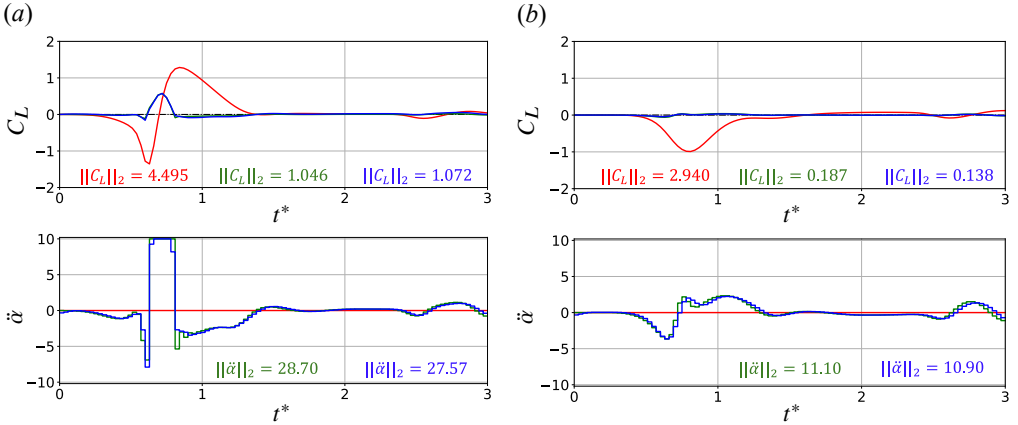


Figure 8: The lift histories and angular acceleration histories under no control, P control ($K_p = 60$), and RL control for representative single-gust case 1 in (a), and representative single-gust case 2 in (b). The color convention is —: no control, —: P control, —: RL control. The corresponding total rewards are: (a) $\sum r_t = -124.54$, $\sum r_t = 82.42$, $\sum r_t = 82.65$; (b) $\sum r_t = 3.96$, $\sum r_t = 97.40$, $\sum r_t = 97.67$.

the strong gust when we implement pitching about the mid-chord. This insight motivates a further investigation about the pivot point location, as we will discuss in §3.3.

We note in passing that, for linear control in this work, we have limited ourselves to proportional control only. It is obviously possible to extend the P control to incorporate additional control terms, such as integral (I) and derivative (D), i.e. PID control. However, for this nonlinear dynamical system the derivation of the control gains requires a complex manual tuning process which cannot be exactly aligned with the reward function structure. In contrast, the RL agent learns the optimal control strategy with respect to the reward function automatically, and this offers a more scalable and adaptive solution that extends to problems with nonlinear dynamics, as we will explore in the following sections.

3.2. Extending control capabilities: mid-chord pitching in multi-gust environment

Having shown the effectiveness of the P control and RL control in a relatively simple environment involving a single gust, we now turn to a more realistic and challenging scenario, characterized by successive gusts. In an ideal setting, one would consider an environment with an infinite sequence of gusts to fully capture the complexity of the real-world disturbances. However, such a setup is computationally infeasible for training, so a reasonable choice of a finite number is necessary. Therefore, we choose to first train the RL agent in environments with up to three successive gusts, and then evaluate the control strategy in environments with up to eight gusts as an approximation of an infinite successive gust environment. This setup is intended to address the following key questions: Does the performance gap between the RL control and the P control widen in the multi-gust environment compared to the gap observed in the single-gust environment, and if so, in what manner? How well do RL control strategies trained in single- or three-gust environments generalize to the more complex eight-gust setting, and does training in a multi-gust environment yield superior performance? By examining these questions, we aim to assess the capability and scalability of the RL control strategies.

The learning envelopes for the RL agent trained in a three-gust environment is depicted in figure 9. Here, P control with gain $K_p = 30$ is selected for pretraining, but we note that other K_p values may also serve effectively as pretraining expert data. We can observe that the

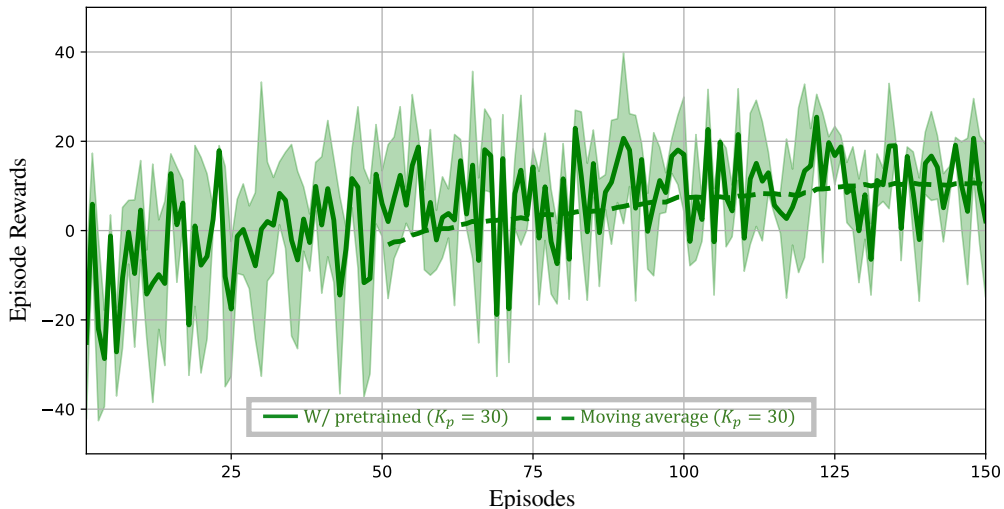


Figure 9: Learning envelopes for mid-chord pitching RL agents in three-gust environment. The solid lines and the shadow regions are the mean and std values of the episode sum rewards across three different runs. For the dashed lines, the moving average has a window size of 50. At each episode index, the episode reward is averaged across all parallel environments per run.

learning starts at an initial reward of around -25 , exhibits a steady improvement, and appears to converge by the 150th episode. By comparing with the learning envelopes in a single-gust environment, the present training curve exhibits a notably larger variance, especially during the early episodes. This variance is reasonable due to the increased complexity and stronger disturbance introduced by three gusts. The converged training curve shows that the RL agent is capable of learning an effective control strategies in a more complex environment, emphasizing the generalizability of the proposed learning framework.

In figure 10 we evaluate the trained RL control strategies against the P control strategies over 45 random cases with three gusts. First, we observe that the case with no control yields a total reward of around -175 , which is significantly lower than the corresponding value of approximately 15 in a single-gust environment and reflects the stronger disturbance introduced by three successive gust. Furthermore, the total reward increases with the K_p value until it reaches the peak total reward of around -14 at $K_p = 70$. Beyond this point, the performance starts to deteriorate, likely due to the system becoming overly reactive to the gust. Meanwhile, the RL agent shows a clear improvement in performance from the initial pretrained policy (blue dashed line) to the final pretrained policy (blue envelope). The final RL control surpasses the best P control by a reward margin of approximately 7. This performance gap is notably larger than the marginal 0.4 improvement observed in the single-gust environment. This improvement supports the hypothesis that the RL control scales better with increased system complexity and nonlinearity compared to proportional control, and thus demonstrates the advantage of the RL approach in a more challenging multi-gust environment.

Similar to §3.1, in figure 11 we select two representative cases to show the corresponding lift and action histories and report the corresponding norms $\|C_L\|_2$ and $\|\ddot{a}\|_2$. The P control corresponds to $K_p = 70$ due to its optimal performance in figure 10. The RL control shows a smaller $\|C_L\|_2$ and $\|\ddot{a}\|_2$ compared to P control in both of the two representative cases, which means that the RL control mitigates the lift tracking error energy better with less control

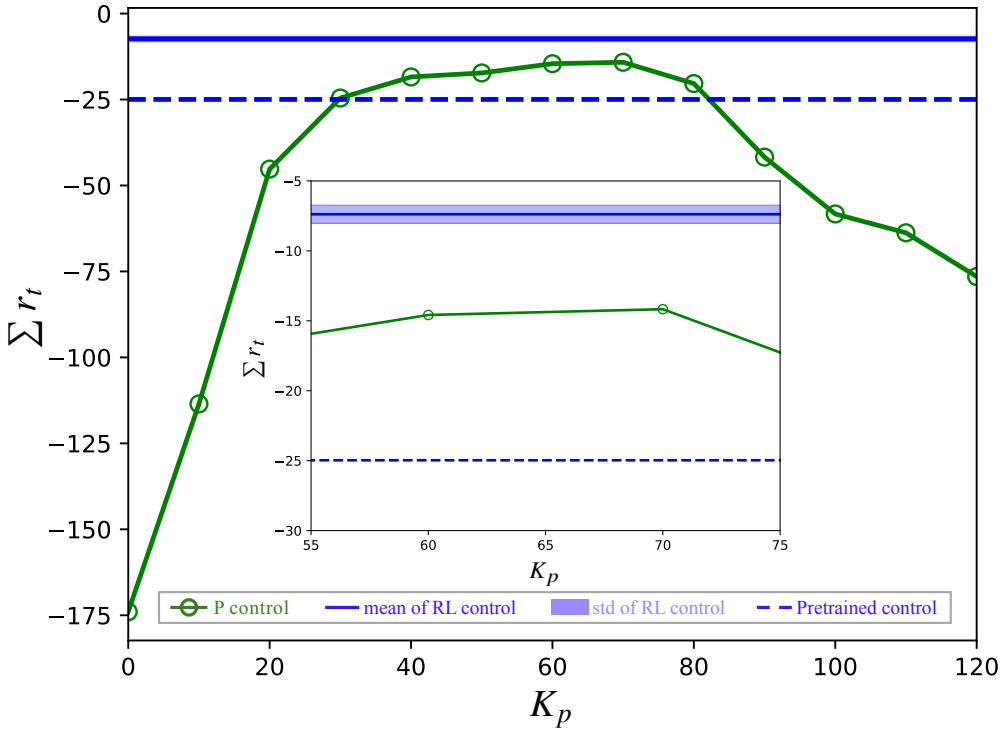


Figure 10: Evaluation of proportional control and RL control in three-gust environment. Each P control data point is averaged over 45 random cases. The mean and standard deviation value for the RL agents are calculated from the last 5 episodes.

effort. Both of these facts contribute to the higher total reward for RL control compared to P control. These improvements are also visually evident in the lift histories. For example, in representative case 1, the lift history under RL control shows a smaller disturbance bump compared to the one under P control at around convective time 2. Similarly, in representative case 2, the RL control results in a smaller lift deviation against P control at convective time approximately 1.2. These improvements likely stem from subtle refinements in the airfoil kinematics, driven by small but effective modifications in the $\tilde{\alpha}$ profile learned by the RL policy. Despite these improvements, we can still see some notable lift variations under the RL control. These remaining deviations are primarily due to the magnitude limit we impose on the $\tilde{\alpha}$, which constrains the ability of the controller to counteract a strong gust. This can be confirmed by the correspondence between the intervals of the notable lift variation and the saturation of $\tilde{\alpha}$ at the upper or lower bounds. Overall, these findings illustrate that, even when the control authority is limited, the RL control can learn to modulate the actuation to extract better performance.

We now turn our attention to the eight-gust environment, which approximates the n -successive gust environment commonly encountered in real-world applications. Figure 12 shows the lift and action histories for a representative eight-gust case under four control strategies: no control, P control, RL control trained in a single-gust environment, and RL control trained in a three-gust environment. Due to the extremely large parameter space associated with the eight-gust setup, performing a comprehensive statistical evaluation—similar to those conducted for the single- and three-gust cases—would require hundreds of simulation runs per control strategy, so it is computationally prohibitive. Therefore, instead of

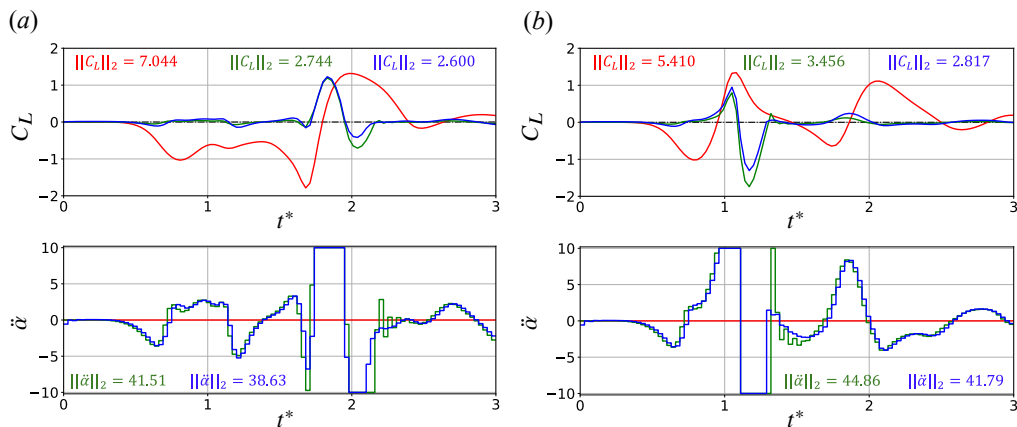


Figure 11: The lift histories and angular acceleration histories under no control, P control, and RL control for representative three-gust case 1 in (a), and representative single-gust case 2 in (b). The color convention is —: no control, —: P control, —: RL control. The corresponding total rewards are: (a) $\sum r_t = -451.24$, $\sum r_t = 4.88$, $\sum r_t = 15.46$; (b) $\sum r_t = -225.16$, $\sum r_t = -43.53$, $\sum r_t = 3.29$.

identifying an optimal K_p through exhaustive evaluation, we adopt a more feasible approach. Considering that the optimal gains in single-gust and three-gust environments are both approximately $K_p = 70$, we simply choose $K_p = 70$ as a reasonable representative value.

Note that the simulation here lasts for 6 convective time units, comprising 200 control steps, so the ideal total reward is 200 if C_L remains zero with no control effort throughout the episode. We can first observe from $\|C_L\|_2$ and $\|\ddot{\alpha}\|_2$ in figure 12 that both RL agents achieve a comparable lift regulation, slightly larger than the P controller but requiring significantly less control effort. Therefore, the total rewards of the two RL agents are higher than the P controller. Notably, we see that the P control exhibits a strong temporal fluctuation in the $\ddot{\alpha}$ history, and this is also reflected somewhat in the corresponding C_L history. This behavior indicates that the P controller tends to overreact to the successive gust disturbances. In addition, by comparing the two RL agents, we find that the RL agent trained in the three-gust environment shows a slightly better lift regulation with less control effort, but the performance gap between them remains modest. This result is somewhat surprising, as we initially expected that the richer dynamics in the three-gust environment—including nonlinear interactions between successive gusts—would provide more informative training and lead to greater generalization capability. This lack of significant difference may be attributed to the magnitude limit we impose on the $\ddot{\alpha}$. In particular, we observe that the RL agent trained in a single-gust environment performs very well during most of the episode except for the time intervals around 0.7 and 3.2, when the lift disturbance remains insufficiently mitigated, and these two time instances both coincide to points when the $\ddot{\alpha}$ is saturated in both controllers. Even with additional training experience, the authority of the mid-chord pitch actuation is limited, and the three-gust RL agent cannot simply apply a stronger control input to suppress the disturbance. Instead, it must improve performance by subtly adjusting preceding control actions to influence the future airfoil kinematics and lift response—a capability that may only provide incremental improvement. Further evidence for the hypothesis will be shown and discussed in §3.4, in which the $\ddot{\alpha}$ for quarter-chord pitching remains unsaturated throughout the episode. Nonetheless, it is noteworthy that the RL agent trained in a three-gust environment achieves a total reward $\sum r_t = 150.77$, so it is reasonable to conclude that the

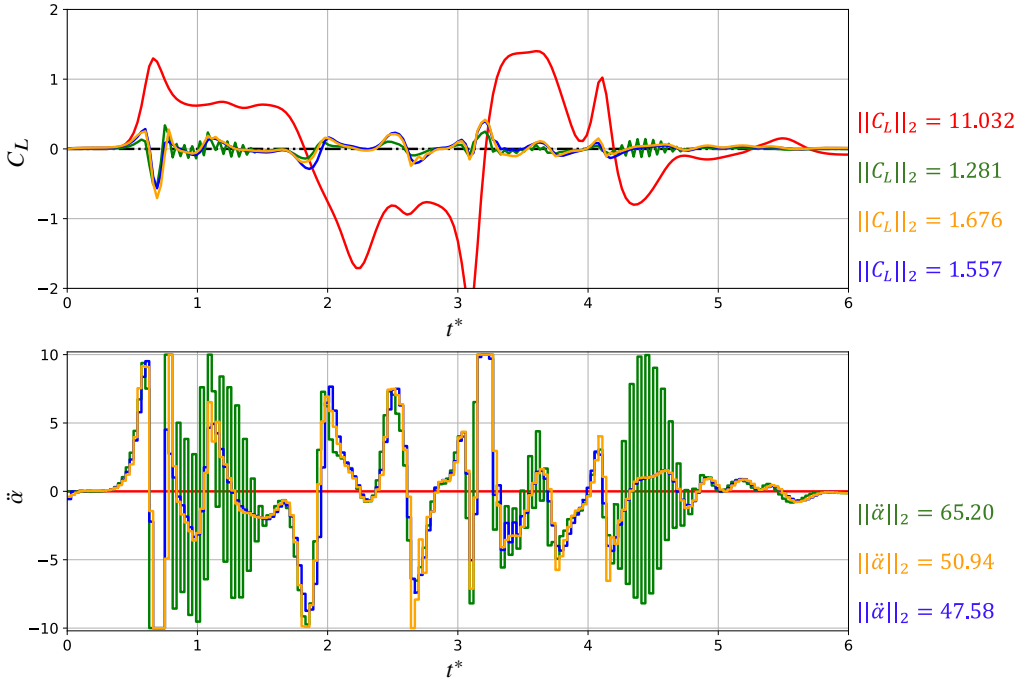


Figure 12: The lift histories and angular acceleration histories under no control, P control, RL control trained from single-gust environment, and RL control trained from three-gust environment for one representative case in eight gust environment. The color convention is **—**: no control, **—**: P control, **—**: RL control trained in single-gust environment, **—**: RL control trained in three-gust environment. The corresponding total rewards are: $\sum r_t = -1152.17$, $\sum r_t = 109.17$, $\sum r_t = 142.84$, $\sum r_t = 150.77$.

RL agent trained in an environment with a finite number of gust can still be an effective control strategy in an environment with an infinite number of gusts.

In summary, our results confirm that the performance gap between RL and P control widens in the multi-gust environment, validating our hypothesis that RL control is more scalable in handling increased system complexity and nonlinearity. Moreover, we observe that both RL agents trained in single- and three-gust environments can be applied to n -successive gusts effectively, and that the RL agent trained in three gusts generalizes slightly better than the one trained on a single gust, but the margin of improvement is moderate due to the actuation magnitude limit. These insights suggest that further performance gains may be achievable with increased control authority, and thus motivate us to examine the effect of pivot point location on control effectiveness in the next sections.

3.3. Revisiting the pivot location: quarter-chord pitching in single-gust environment

The previous results highlighted that, while RL control in a mid-chord pitching configuration can effectively mitigate lift variation, its performance may be limited by the imposed $\ddot{\alpha}$ constraint. To explore whether an alternative pivot point location can improve the control performance, we now revisit the pitching configuration and shift the pivot point to the quarter-chord location. This is a classical choice in unsteady aerodynamic flow, so we expect it to provide an effective control strategy. Before we explore the n -successive gust scenario, it is prudent to first investigate the single-gust environment.

The lift on an airfoil encountering a gust and pitching about zero angle of incidence can

	P control $K_p = 0$	P control $K_p = 1$	P control $K_p = 2$	P control $K_p = 3$	P control $K_p = 4$	RL agents mean	RL agents std
$\sum r_t$	16.64	53.71	74.29	-14599.92	-18998.54	90.33	0.64

Table 3: For quarter-chord pitching, evaluation of the P control with different gains and RL control over 15 random cases.

be decomposed into three terms:

$$C_L = C_{L_{\text{am}}} + C_{L_g} + C_{L_c}, \quad (3.2)$$

where $C_{L_{\text{am}}}$ represents the inertial reaction (i.e., added mass) of the fluid due to airfoil acceleration, C_{L_g} represents the contribution from the gust with no control (i.e., on the airfoil at zero angle of attack), and the remaining lift C_{L_c} approximately represents the aerodynamic response to the gust due to pitching kinematics (through the kinematics' modification of fluid vorticity).

We define the first of these, the added mass contribution, using potential flow theory (Eldredge 2019):

$$C_{L_{\text{am}}} = \underbrace{\frac{\pi c d}{2U_\infty^2} \ddot{\alpha} \cos \alpha}_{C_{L_{\ddot{\alpha}}}} + \underbrace{\frac{-\pi c}{2U_\infty} \dot{\alpha} \cos 2\alpha}_{C_{L_{\dot{\alpha}}}}, \quad (3.3)$$

where d is the distance between the pivot point and mid-chord point, defined as positive if the pivot is downstream of the mid-chord and negative if it is upstream. For the mid-chord pitching pursued in the previous sections, $C_{L_{\ddot{\alpha}}} = 0$ due to $d = 0$; in contrast, for the quarter-chord pitching studied in this section, $d = -c/4$. We note again that the pitching kinematics in this study is defined as positive for counter-clockwise rotation.

Interpreted in this decomposition, our objective for maintaining zero lift is equivalent to controlling the airfoil so that $C_{L_{\text{am}}} + C_{L_c}$ compensates the effect from the gust, C_{L_g} . In the previous mid-chord pitching configuration, the only available terms for control are $C_{L_{\dot{\alpha}}}$ and C_{L_c} . It is important to note that neither of the two terms is directly dependent on the control input $\ddot{\alpha}$, but only on its integral $\dot{\alpha}$, so the controller is somewhat limited in its authority. In contrast, the quarter-chord pitching configuration also provides access to $C_{L_{\ddot{\alpha}}}$ for control, empowering the controller with more flexibility and higher responsiveness by adjusting this term directly. As we will show in subsequent results, $\dot{\alpha}$ is often smaller by an order of magnitude than $\ddot{\alpha}$ under various control strategies, which suggests that the actuation may not be as likely to saturate at the magnitude constraint in the quarter-chord pitching configuration.

However, the increased responsiveness also raises a challenge: the P control that is suitable in the mid-chord pitching configuration now may overreact to the lift disturbance in this quarter-chord configuration, and therefore cannot be easily leveraged for pretraining the RL controller. This overreaction is due to the fact that the angular acceleration obtained from the control law (3.1) is one control step later than the measured lift from which it is determined, while the lift $C_{L_{\ddot{\alpha}}}$ is instantaneously dependent on the angular acceleration. An evaluation of the P control with different gains is provided in table 3. At large K_p , the controller incurs a very large negative reward, indicating exceptionally poor performance that is primarily penalized by the quadratic lift term. At small gain K_p it is possible to maintain a stable lift history, and the total reward $\sum r_t = 74.29$ at $K_p = 2$ seems to indicate good performance. However, we will show later in figure 14 that this high reward is attributable more to the small magnitude of the $\ddot{\alpha}$ rather than successful lift regulation.

The small K_p controller also leads to expert data with minimal action variation, which, when used as pretraining data, offers little advantage over the default (random) initialization of the RL policy network. Specifically, since we use zero-center initialization (a standard PyTorch initialization (Paszke *et al.* 2019)) for the policy networks, which produces a near-zero output already, and we employ a fixed initial policy standard deviation of 1, which allows for substantial exploration early in training, the influence of the expert data is diminished during initial policy updates. Therefore, we chose not to use pretraining in this case. To clarify, our decision to omit pretraining in this configuration is not a limitation of the framework, but rather a deliberate design choice driven by the observed ineffectiveness of expert data in this particular setup. As we will demonstrate, even without pretraining, the RL agent is capable of learning an effective control strategy in the quarter-chord configuration. For the readers who may be interested in pursuing pretraining under these conditions, one potential solution is to develop a full PID controller, which would likely be more successful than P control in reducing the overreaction. One could also apply a scaling factor to amplify the action magnitudes from the expert data before using them for pretraining, which would ensure that the pretrained policy deviates more meaningfully from the zero-center initialized baseline. Another approach may be to employ a smaller initial policy standard deviation, which would constrain the exploration range and help maintain the influence of the pretrained expert data. However, these approaches require careful tuning, and are outside the scope of the present study.

The learning curve for the RL agent in the quarter-chord pitching configuration is depicted in figure 13. We observe that the learning process starts from an initial reward around -1000 , which is much smaller than -430 in the mid-chord pitching from figure 6. This reflects the unstable lift profile caused by the added-mass term $C_{L\ddot{\alpha}}$ during the early stages of the training. As training proceeds, the reward grows steadily with a decreasing variance, and reaches 0 at approximately the 300th episode. Beyond this point, the learning proceeds relatively more slowly, and finally reaches around 80. While the learning curve suggests that the policy may continue to improve marginally, we opt to stop training at this stage to avoid unnecessary computational cost, as the remaining improvements are likely negligible. Based on the final performance of around 80, which is much larger than 60 for the performance of mid-chord RL control shown in figure 6, we can already conclude that the quarter-chord RL control is superior.

The evaluation of the performance of the RL agents from the last 5 episodes is illustrated in table 3. The RL agents outperform the best P control with a performance gap of around 16, which is much larger than the gap observed in the mid-chord pitching configuration. To provide further insight, figure 14 presents the lift and action histories for one representative case. For clarity, the P control shown corresponds to $K_p = 2$, which yields the highest performance among the tested gains. From the report of $\|C_L\|_2$ and $\|\ddot{\alpha}\|_2$, we can first see that quarter-chord pitching RL control regulates lift much better than quarter-chord P control, and with only slightly more control effort. Consequently, the quarter-chord RL control has a much higher total reward. Furthermore, a comparison between the mid-chord and quarter-chord RL controllers highlights the benefits of the pivot point shift. We can see that the quarter-chord pitching results in a better lift tracking with significantly less control effort. The lift bump under mid-chord RL control at convective time around 0.75 is absent in the profile under quarter-chord RL control. This aligns with our earlier discussion that the presence of the $C_{L\ddot{\alpha}}$ term in the quarter-chord setup grants the controller direct authority over lift regulation via angular acceleration. As a result, the quarter-chord RL controller does not encounter saturation of $\ddot{\alpha}$, avoiding the performance limitations seen in the mid-chord case.

For more specific comparison between the mid-chord and quarter-chord RL control on the basis of flow physics, we present the decomposed lift components based on equations

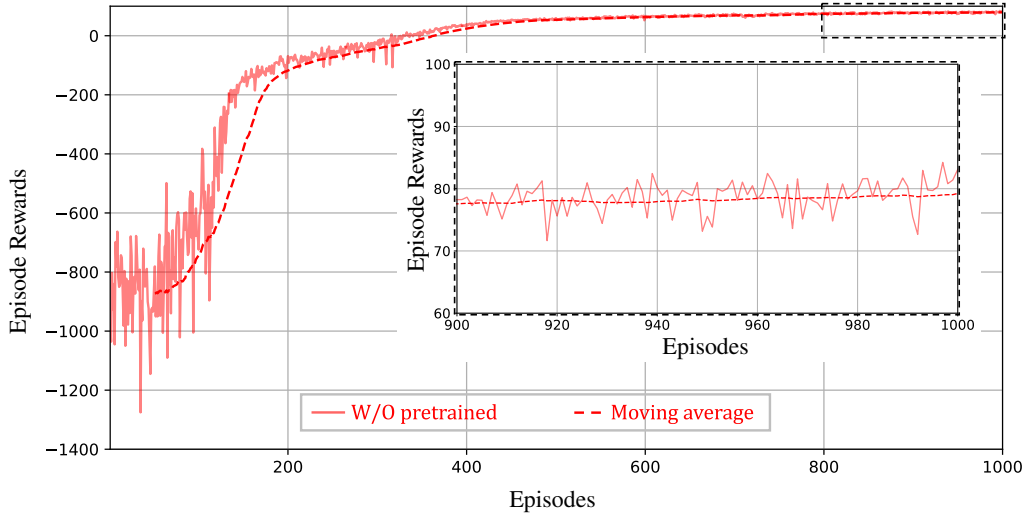


Figure 13: Learning curve for quarter-chord pitching RL agents in single-gust environment. The solid line represents the history of episode rewards for single run. The dashed line is the moving average with a window size of 50. At each episode index, the episode reward is averaged across all parallel environments.

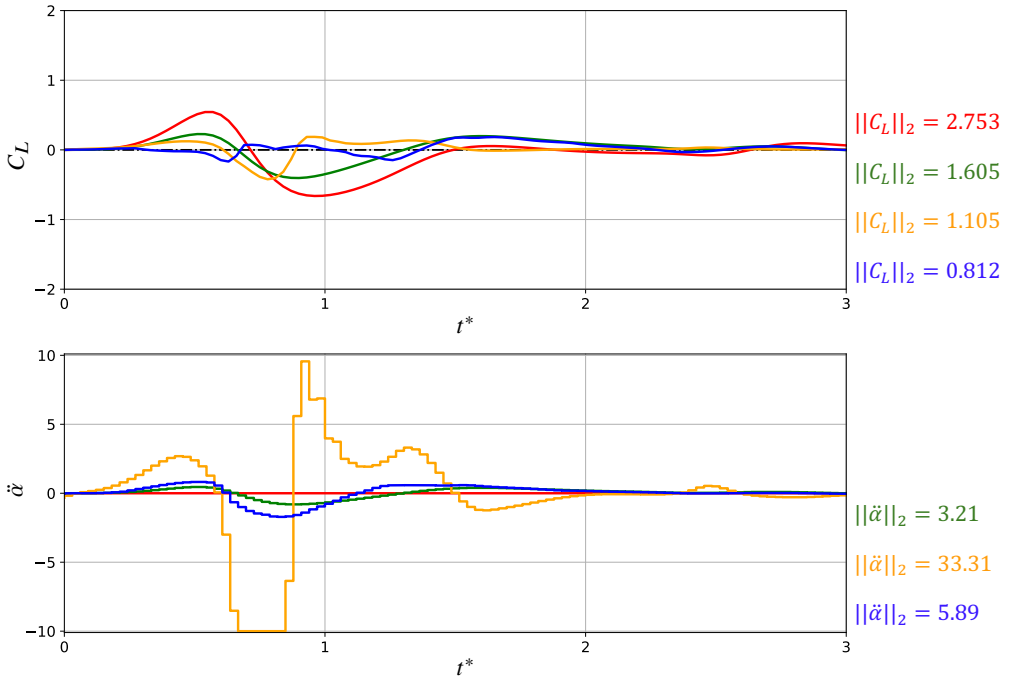


Figure 14: The lift histories and angular acceleration histories: under no control, quarter-chord P control, mid-chord RL control, and quarter-chord RL control for one representative case in single-gust environment. The color convention is —: no control, —: quarter-chord P control, —: mid-chord RL control, —: quarter-chord RL control. The corresponding total rewards are: $\sum r_t = 15.78$, $\sum r_t = 71.02$, $\sum r_t = 81.22$, $\sum r_t = 92.02$.

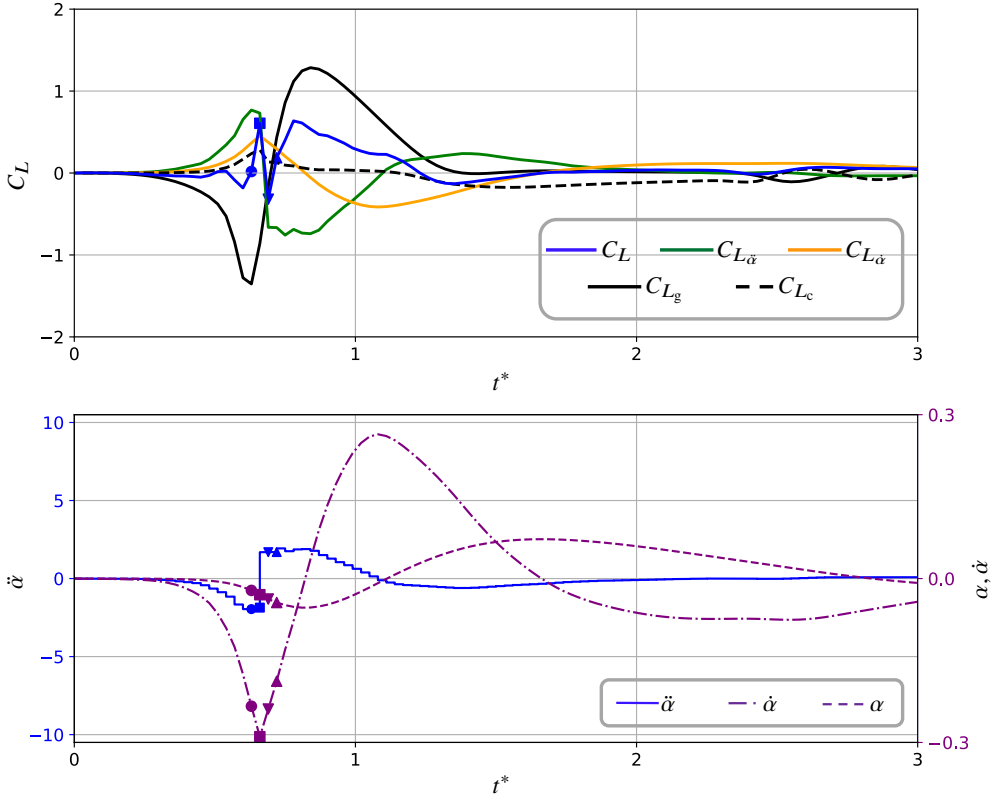


Figure 15: Lift decomposition for one representative case in quarter-chord pitching configuration.

(3.2) and (3.3), along with the corresponding pitching kinematics histories, for an identical representative case. The results for the quarter-chord and mid-chord configurations are shown in figures 15 and 17, respectively. The corresponding vorticity contours and surface pressure distribution for the two configurations at specific time instances ($t^* = 0.6, 0.63, 0.66, 0.69$), which correspond to four consecutive control steps, are shown in figures 16 and 18, respectively.

From the comparison between figures 15 and 17, we can first observe that the quarter-chord RL control can leverage $C_{L_{\dot{\alpha}}}$ to compensate for C_{L_g} , so that $C_{L_{\dot{\alpha}}}$ and C_{L_c} magnitudes are relatively smaller than they are for mid-chord pitching. This can also be observed from the magnitudes of the $\dot{\alpha}$ and α in the quarter-chord pitching configuration: both quantities' magnitudes are bounded by 0.3, much smaller than 1.2 in the mid-chord pitching configuration. The smaller magnitudes of $\dot{\alpha}$ and α directly correspond to smaller $C_{L_{\dot{\alpha}}}$ in quarter-chord pitching. They also reveal the reason why C_{L_c} remains small, since a smaller change of pitching kinematics leads to a smaller modification to the vorticity distribution compared to the uncontrolled flow. The events in the interval around $t^* = 0.6$ provide a specific illustration of these differences. We notice that both RL agents are pitching up (clockwise angular velocity) during this interval, but the mid-chord RL agent opts to decelerate beyond $t^* = 0.6$, while the quarter-chord RL agent chooses to decelerate one step later, i.e., at $t^* = 0.63$. This difference is due to the fact that the mid-chord RL agent needs more time to compensate for the gust, C_{L_g} , by modifying $C_{L_{\dot{\alpha}}}$ and C_{L_c} via $\dot{\alpha}$ and α , which are integrals of the action (the angular acceleration). In contrast, the quarter-chord RL agent is

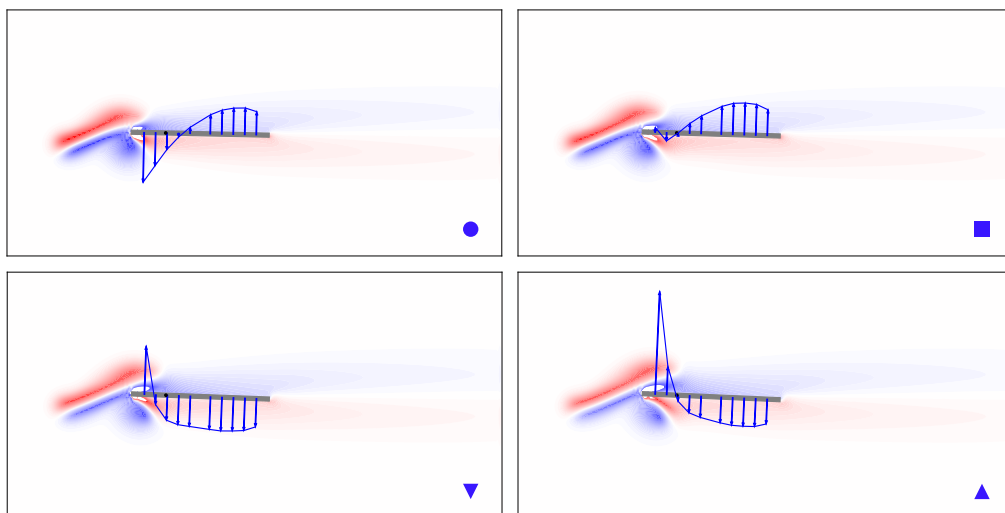


Figure 16: The corresponding vorticity contour and surface pressure distribution at the four steps indicated in figure 15. $C_{\Delta p}$ is scaled $\frac{1}{4}$ from its original value.

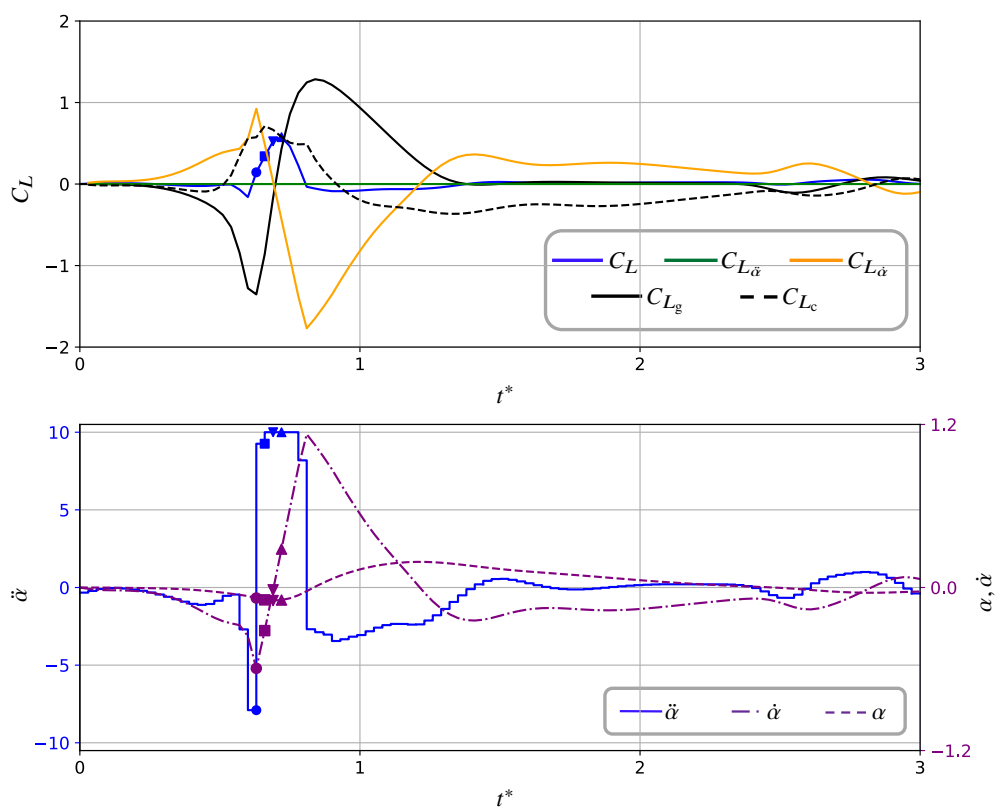


Figure 17: Lift decomposition and the corresponding action history for one representative case in mid-chord pitching configuration.

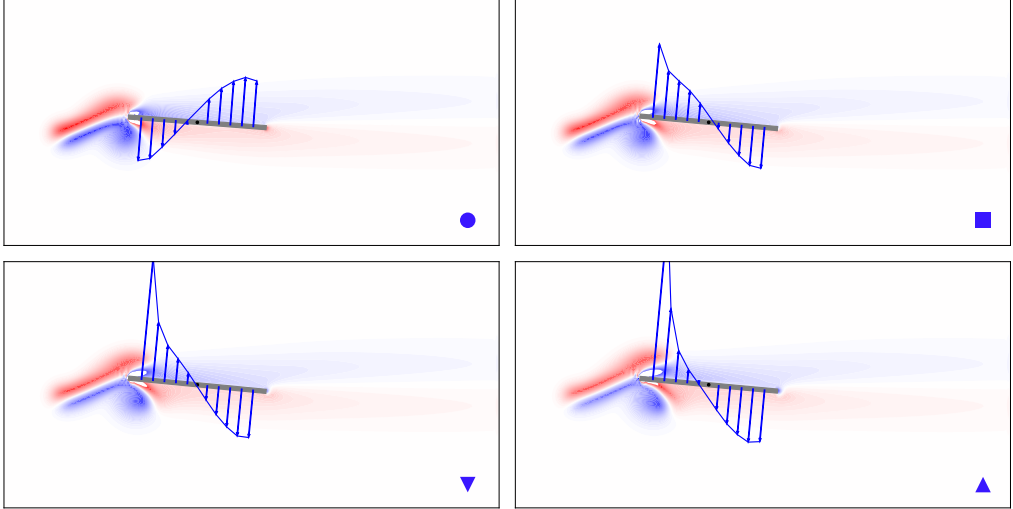


Figure 18: The corresponding vorticity contour and surface pressure distribution at the four steps indicated in figure 17. $C_{\Delta p}$ is scaled $\frac{1}{4}$ from its original value.

less restricted, since it can react through $C_{L_{\ddot{\alpha}}}$, and can do so with a discontinuous change in angular acceleration. In summary, in the quarter-chord pitching configuration, the $C_{L_{am}}$ plays the dominant role for compensating for C_{L_g} , but $C_{L_{am}}$ and the C_{L_c} are equivalently important (and less responsive) in mid-chord pitching configuration.

By comparing the pressure and vorticity for the controllers in figures 16 and 18, we find that both RL agents effectively learn to counteract the effect of the gust on the pressure near the leading edge by leveraging pitching to modify the overall surface pressure. However, they show important differences in how they achieve this. In the mid-chord configuration, the RL agent reverses the direction of angular acceleration $\ddot{\alpha}$ while the leftmost pressure sensor still reads a negative value, indicating a more anticipatory control behavior. In contrast, the quarter-chord RL agent initiates the change in $\ddot{\alpha}$ only after the leftmost pressure sensor signal turns positive. This behavioral difference may be attributed to the additional control authority provided by the $C_{L_{\ddot{\alpha}}}$ term in the quarter-chord configuration as we discussed above, allowing the agent to respond more reactively without requiring as much lead time. However, since the input to the transformer-based policy network consists of a temporal window of past observations, a more detailed investigation than we present in this paper is needed to fully understand how the pressure history is being mapped to the angular acceleration output, and how this mapping differs across pivot configurations.

3.4. Transferring control strategies: quarter-chord pitching in multi-gust environment

Having established an effective control strategy for the quarter-chord pitching configuration in the single-gust environment, we now extend our investigation to a more realistic and challenging scenario involving a n -successive gust. As we have discussed in §3.3, the P control cannot provide us with suitable expert data for pretraining to accelerate the RL training process in the quarter-chord pitching configuration. However, training from scratch in the single-gust environment required ~ 1000 episodes, as shown in figure 13. Therefore, it is computationally infeasible to train the RL agent from scratch in a more complex environment with multiple gusts, as it would require even more episodes to converge. In order to overcome this difficulty, we leverage transfer learning to make the training feasible. Specifically, we treat the previous single-gust environment as the source task, where the RL agent has acquired

useful knowledge about the fluid dynamics and control principles. This knowledge is then transferred to the multi-gust environment—our target task—serving as a warm start that accelerates learning and facilitates adaptation to the more complex setting.

The learning curve for the transferred RL agent in a three-gust environment is shown in figure 19. The initial reward is around 20, which indicates that the RL agent trained on a single gust generalizes moderately well to the more complex task. A sharp drop occurs in the first 20 episodes, but then recovers steadily. This sudden drop is characteristic of transfer learning in actor–critic architectures: the policy network may carry over useful features from the source task, but the value network often suffers from inaccurate approximation due to the environment shift between tasks. As a result, early updates primarily focus on correcting the value approximation, rather than improving the control policy, since a large value loss may dominate the total loss function (see equation (2.14)). After this correction phase, the agent resumes improving the policy, surpassing its initial performance at around episode 350 and eventually reaching a final reward close to 80, which is comparable to the final performance in the single-gust environment. This comparable performance is surprising given the increased task complexity. We hypothesize two reasons: First, the richer gust structure in the three-gust environment provides the RL agent with more diverse training signals, potentially enabling it to learn more generalizable or refined control strategies than what the single-gust setup affords. Second, the quarter-chord configuration allows sufficient actuation authority such that the angular acceleration constraint does not limit control performance. Consequently, the RL agent retains the capability to mitigate the stronger disturbance introduced by three gusts without degradation in performance. We note that the learning curve in figure 19 is not yet fully converged, but we choose to stop the training here, anticipating that the subsequent improvement will be small. Compared to the ~ 1000 episodes required to train the RL agent from scratch in a single-gust environment, training in this more complex environment with transfer learning only takes ~ 500 episodes. Given the increased task complexity, training from scratch in the multi-gust setting would likely require substantially more than 1000 episodes to reach comparable performance. Therefore, this result demonstrates that transfer learning effectively accelerates the training process and leads to substantial savings in computational resources.

After the training process, we now evaluate and compare the RL agents in the two different pivot configurations on a representative case in the three-gust environment in figure 20. From the $\|C_L\|_2$ and $\|\ddot{\alpha}\|_2$ comparison, quarter-chord RL control regulates lift better than mid-chord RL control, and with significantly less control effort. Therefore, the total reward for quarter-chord RL control is much higher than the one for mid-chord RL control. Additionally, the lift bumps under mid-chord RL control due to the actuation constraint almost disappear in the lift history under quarter-chord RL control, verifying that the quarter-chord pivot configuration offers the RL agent more control authority even in the more complex environment.

Finally, we turn our attention to the more realistic and challenging case, approximating the n -successive gust scenario. We apply the agents trained for quarter-chord pitch control in the single- and three-gust environments, respectively, to an eight successive gust environment. As we have discussed in §3.2, the vast parameter space of eight gust renders an exhaustive statistical evaluation infeasible, so we limit our analysis to a representative case to gain insight into the control effectiveness, as shown in figure 21. Since the simulation for this case lasts 6 convective time units (200 control steps), the ideal total reward is 200 when zero lift is achieved without control effort for every control step. First, the $\|C_L\|_2$ and $\|\ddot{\alpha}\|_2$ indicate that the RL agent trained in the three-gust environment can mitigate the lift variation much better than one trained in a single-gust environment, with only marginally more control effort. As a result, the total reward for the RL agent trained in the three-gust environment is much

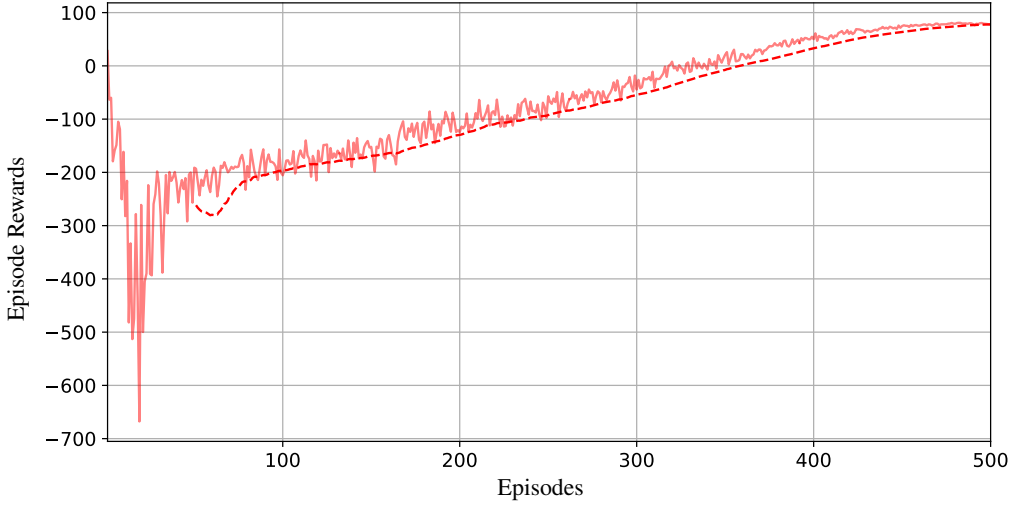


Figure 19: Learning curve for quarter-chord pitching RL agents in three-gust environment. The solid line represents the history of episode rewards for single run. For the dashed lines, the moving average has a window size of 50. At each episode index, the episode reward is averaged across all parallel environments.

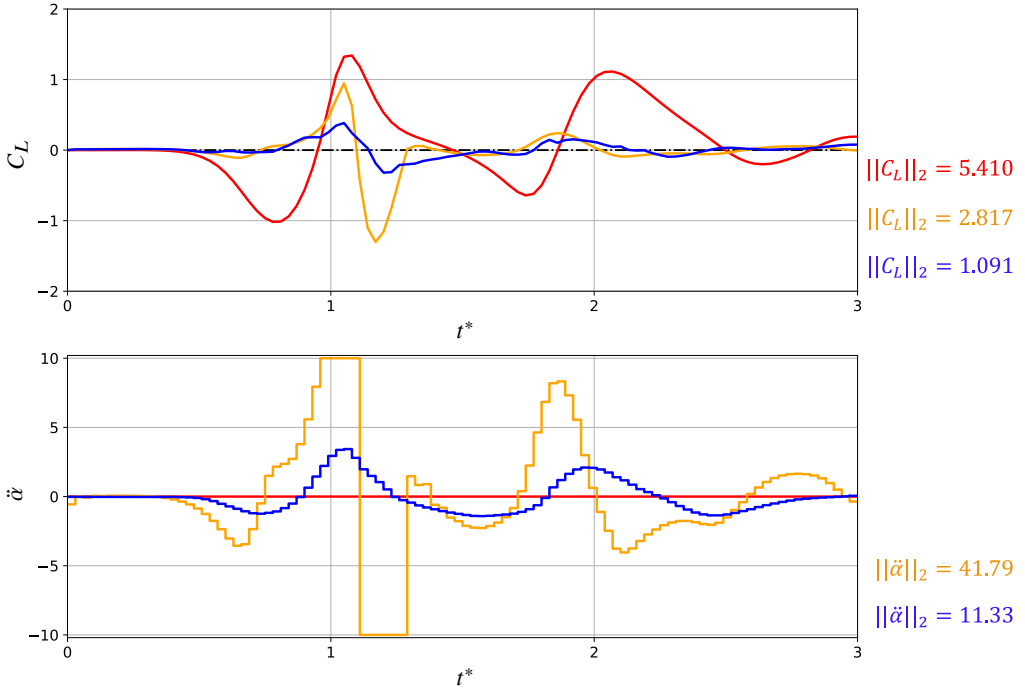


Figure 20: The lift histories and angular acceleration histories under no control, mid-chord RL control, and quarter-chord RL control for one representative case in three-gust environment. The color convention is —: no control, —: mid-chord RL control, —: quarter-chord RL control. The corresponding total rewards are: $\sum r_t = -225.16$, $\sum r_t = 3.29$, $\sum r_t = 84.86$.

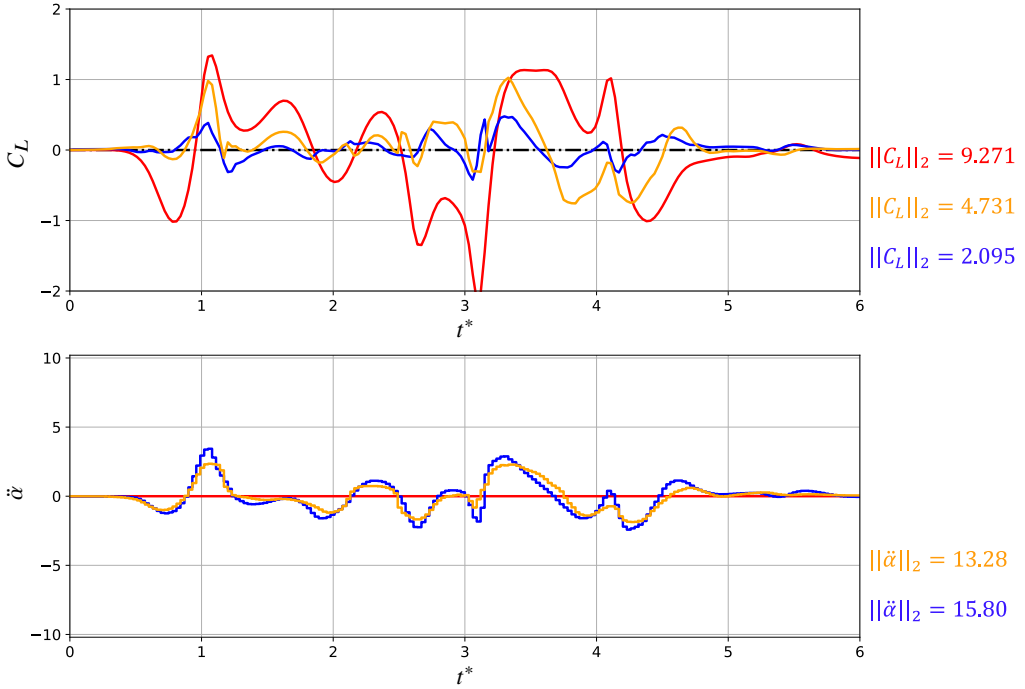


Figure 21: The lift histories and angular acceleration histories under no control, RL control trained from single-gust environment, and RL control trained from three-gust environment for one representative case in eight gust environment. Both RL controls are under quarter-chord pitching configuration. The color convention is —: no control, —: RL control trained in single-gust environment, —: RL control trained in three-gust environment. The corresponding total rewards are: $\sum r_t = -754.95$, $\sum r_t = -51.42$, $\sum r_t = 146.98$.

higher than the one for RL agent trained in the single-gust environment. Additionally, we find once again the familiar result that RL control in a quarter-chord pitching configuration has a higher control authority than mid-chord pitching, so that its control capability is not affected by the magnitude limit of the actuation, even in this more complex eight-gust environment. Furthermore, the RL agent trained in the three-gust environment exhibits a refined control strategy: although the angular acceleration profile shows only moderate adjustments in magnitude compared to the single-gust agent, the resulting lift response is significantly improved. This suggests that the agent has learned to leverage all lift components more effectively to compensate for interacting gust disturbances. Lastly, considering that the RL agent trained in the three-gust environment has achieved a total reward of $\sum r_t = 146.98$, comparable to the ideal total reward of 200, we can conclude that the control strategy learned in the environment involving a finite number of gusts can be effectively applied to the environment with an infinite number of gusts.

4. Conclusions

In this study, we have sought an effective pitch control strategy for lift regulation when a flat plate airfoil encounters an arbitrarily long sequence of gust disturbances and investigated the effect of the pivot location on the control performance and the accompanying flow response.

We have proposed a transformer-based RL framework to deal with the POMDP challenge that is common in flow control problems. In light of the potentially expensive training cost

of RL for such problems, we have also proposed two approaches that can accelerate the RL training process: pretraining and transfer learning. We have demonstrated the effectiveness of these acceleration methods in two flow control scenarios. In a mid-chord pitching configuration, we have employed P control to generate expert data for pretraining and shown that the subsequent RL training converges much faster than training from scratch. In a quarter-chord pitching configuration, we have accelerated the RL training in a three-gust environment by transferring the knowledge that the RL agent learns in a single-gust environment.

We have found that P control is an effective control strategy in the mid-chord pitching configuration on its own, but that the performance improvement that RL control exhibits over P control widens for multiple-gust scenarios, suggesting that RL control is more scalable in handling system complexity and nonlinearity. In the quarter-chord pitching configuration, we have found that the RL control significantly outperforms the P control, even in a single-gust environment. Furthermore, we have shown that, in either pivot configuration, an RL control strategy learned in an environment with a finite sequence of gusts can be translated effectively into an environment with an arbitrarily long sequence of gusts.

By comparing the two pivot configurations, we have shown that the quarter-chord pitching control strategy can achieve superior lift regulation with significantly less control effort than the mid-chord pitching control strategy. Through the decomposition of the lift coefficient into $C_{L_{am}}$ (added-mass effect), C_{L_g} (gust effect under no control), and C_{L_c} (gust response under control), we have revealed that this advantage derives from the term $C_{L_{\dot{\alpha}}}$ in the added-mass component, where it dominates the lift contribution in quarter-chord pitching but is unavailable in mid-chord pitching. In the latter configuration, the agent can only act through $C_{L_{\dot{\alpha}}}$ and C_{L_c} , which are comparable in magnitude to each other, but less responsive than $C_{L_{\dot{\alpha}}}$. This difference provides more control authority in the quarter-chord pivot configuration, and thus addresses the actuation saturation problem observed in mid-chord pitching control.

The present study shows the feasibility of the transformer-based RL, with incorporation pretraining and transfer learning to accelerate training, for control of a highly disturbed flow. However, there are many ways in which the present study can be expanded in future work. For example, we do not investigate the effect of the observation history length, nor the number and locations of the pressure sensors, on the control performance. Additionally, other types of control input (e.g., synthetic jet) and/or other objectives (e.g., drag reduction, non-zero target lift) can be investigated by following the same methodology. These studies could address the underlying question of controllability, which we have not explored in this work. Finally, a further tuning of the hyper-parameters in the present study may be necessary to achieve a higher training efficiency if we intend to investigate even more computationally demanding scenarios, such as lift regulation for a three-dimensional finite-span wing.

REFERENCES

- AN, XUANHONG, WILLIAMS, DAVID R., ELDREDGE, JEFF D. & COLONIUS, TIM 2016 Modeling dynamic lift response to actuation. In *54th AIAA Aerospace Sciences Meeting*. AIAA 2016-0058.
- ÅSTRÖM, K. J. 1965 Optimal control of Markov processes with incomplete state information. *Journal of Mathematical Analysis and Applications* **10** (1), 174–205.
- BECKERS, DIEDERIK & ELDREDGE, JEFF D. 2024 Deep reinforcement learning of airfoil pitch control in a highly disturbed environment using partial observations. *Phys. Rev. Fluids* **9**, 093902.
- BOZINOVSKI, STEVO 2020 Reminder of the first paper on transfer learning in neural networks, 1976. *Informatica* **44**, 291–302.
- BRUNTON, STEVEN L. & ROWLEY, CLARENCE W. 2013 Empirical state-space representations for Theodorsen’s lift model. *Journal of Fluids and Structures* **38**, 174–186.
- BRUNTON, STEVEN L., ROWLEY, CLARENCE W. & WILLIAMS, DAVID R. 2013 Reduced-order unsteady aerodynamic models at low Reynolds numbers. *Journal of Fluid Mechanics* **724**, 203–233.

- DAWSON, SCOTT T., SCHIAVONE, NICOLE K., ROWLEY, CLARENCE W. & WILLIAMS, DAVID R. 2015 A data-driven modeling framework for predicting forces and pressures on a rapidly pitching airfoil. In *45th AIAA Fluid Dynamics Conference*. AIAA 2015-2767.
- ELDREDGE, J. D. 2019 *Mathematical Modeling of Unsteady Inviscid Flows, Interdisciplinary Applied Mathematics*, vol. 50. Springer.
- ELDREDGE, JEFF D. 2022 A method of immersed layers on Cartesian grids, with application to incompressible flows. *Journal of Computational Physics* **448**, 110716.
- ELDREDGE, JEFF D. & JONES, ANYA R. 2019 Leading-edge vortices: Mechanics and modeling. *Annual Review of Fluid Mechanics* **51** (Volume 51, 2019), 75–104.
- FAN, DIXIA, YANG, LIU, WANG, ZHICHENG, TRIANTAFYLLOU, MICHAEL S. & KARNIADAKIS, GEORGE EM 2020 Reinforcement learning for bluff body active flow control in experiments and simulations. *Proceedings of the National Academy of Sciences* **117** (42), 26091–26098.
- FRANCOIS-LAVET, VINCENT, RABUSSEAU, GUILLAUME, PINEAU, JOELLE, ERNST, DAMIEN & FONTENEAU, RAPHAEL 2019 On overfitting and asymptotic bias in batch reinforcement learning with partial observability, arXiv: 1709.07796.
- FUKAMI, KAI & TAIRA, KUNIHICO 2023 Grasping extreme aerodynamics on a low-dimensional manifold. *Nature Communications* **14** (1), 6480.
- GOMAN, M. & KHRABROV, A. 1994 State-space representation of aerodynamic characteristics of an aircraft at high angles of attack. *Journal of Aircraft* **31** (5), 1109–1115.
- HASEGAWA, KAZUTO, FUKAMI, KAI, MURATA, TAKAOKI & FUKAGATA, KOJI 2020 CNN-LSTM based reduced order modeling of two-dimensional unsteady flows around a circular cylinder at different Reynolds numbers. *Fluid Dynamics Research* **52** (6), 065501.
- HEMATI, MAZIAR S., DAWSON, SCOTT T. M. & ROWLEY, CLARENCE W. 2017 Parameter-varying aerodynamics models for aggressive pitching-response prediction. *AIAA Journal* **55** (3), 693–701.
- HOCHREITER, SEPP & SCHMIDHUBER, JÜRGEN 1997 Long short-term memory. *Neural Computation* **9** (8), 1735–1780.
- HOU, WEI, DARAKANANDA, DARWIN & ELDREDGE, JEFF D. 2019 Machine-learning-based detection of aerodynamic disturbances using surface pressure measurements. *AIAA Journal* **57** (12), 5079–5093.
- JONES, ANYA R. 2020 Gust encounters of rigid wings: Taming the parameter space. *Phys. Rev. Fluids* **5**, 110513.
- JONES, ANYA R., CETINER, OKSAN & SMITH, MARILYN J. 2022 Physics and modeling of large flow disturbances: Discrete gust encounters for modern air vehicles. *Annual Review of Fluid Mechanics* **54** (Volume 54, 2022), 469–493.
- KAELBLING, LESLIE PACK, LITTMAN, MICHAEL L. & CASSANDRA, ANTHONY R. 1998 Planning and acting in partially observable stochastic domains. *Artificial Intelligence* **101** (1), 99–134.
- KERSTENS, WESLEY, PFEIFFER, JENS, WILLIAMS, DAVID, KING, RUDIBERT & COLONIUS, TIM 2011 Closed-loop control of lift for longitudinal gust suppression at low Reynolds numbers. *AIAA Journal* **49** (8), 1721–1728.
- KÜSSNER, HANS G. 1932 Stresses produced in airplane wings by gusts. *Tech. Rep.* 645. NACA.
- LAGHARI, ASIF A., JUMANI, AWAIS K., LAGHARI, RASHID A. & NAWAZ, HAQUE 2023 Unmanned aerial vehicles: A review. *Cognitive Robotics* **3**, 8–22.
- LINOT, ALEC J, ZENG, KEVIN & GRAHAM, MICHAEL D 2023 Turbulence control in plane couette flow using low-dimensional neural ode-based models and deep reinforcement learning. *International Journal of Heat and Fluid Flow* **101**, 109139.
- LIU, ZHECHENG, BECKERS, DIEDERIK & ELDREDGE, JEFF D. 2025 Model-based reinforcement learning for control of strongly disturbed unsteady aerodynamic flows. *AIAA Journal* .
- MA, ZHANHUA, AHUJA, SUNIL & ROWLEY, CLARENCE W. 2011 Reduced-order models for control of fluids using the eigensystem realization algorithm. *Theoretical and Computational Fluid Dynamics* **25** (1), 233–247.
- MOUSAVI, HANIEH & ELDREDGE, JEFF D. 2025 Low-order flow reconstruction and uncertainty quantification in disturbed aerodynamics using sparse pressure measurements, arXiv: 2501.03406.
- NARAYANAN, SHRIVATHSAN & GOVINDARAJAN, BHARATH 2024 Effects of gust on the aerodynamics of multi-rotors. *Physics of Fluids* **36** (12), 127169.
- NOVATI, GUIDO, VERMA, SIDDHARTHA, ALEXEEV, DMITRY, ROSSINELLI, DIEGO, VAN REES, WIM M. & KOUMOUTSAKOS, PETROS 2017 Synchronisation through learning for two self-propelled swimmers. *Bioinspiration & Biomimetics* **12** (3), 036001.

- ODUYELA, ADETUNJI & SLEGGERS, NATHAN 2014 Gust mitigation of micro air vehicles using passive articulated wings. *The Scientific World Journal* **2014** (1), 598523.
- PASZKE, ADAM, GROSS, SAM, MASSA, FRANCISCO, LERER, ADAM, BRADBURY, JAMES, CHANAN, GREGORY, KILLEEN, TREVOR, LIN, ZEMING, GIMELSHEIN, NATALIA, ANTIGA, LUCA, DESMAISON, ALBAN, KÖPF, ANDREAS, YANG, EDWARD, DeVITO, ZACH, RAISON, MARTIN, TEJANI, ALYKHAN, CHILAMKURTHY, SASANK, STEINER, BENOIT, FANG, LU, BAI, JUNJIE & CHINTALA, SOUMITH 2019 Pytorch: An imperative style, high-performance deep learning library, arXiv: 1912.01703.
- RABAULT, JEAN, KUČHTA, MIROSLAV, JENSEN, ATLE, RÉGLADE, ULYSSE & CERARDI, NICOLAS 2019 Artificial neural networks trained through deep reinforcement learning discover control strategies for active flow control. *Journal of Fluid Mechanics* **865**, 281–302.
- RENN, PETER I. & GHARIB, MORTEZA 2022 Machine learning for flow-informed aerodynamic control in turbulent wind conditions. *Communications Engineering* **1**, 45.
- ROWLEY, CLARENCE W. 2005 Model reduction for fluids, using balanced proper orthogonal decomposition. *International Journal of Bifurcation and Chaos* **15** (03), 997–1013.
- RUMELHART, DAVID E., HINTON, GEOFFREY E. & WILLIAMS, RONALD J. 1986 Learning representations by back-propagating errors. *Nature* **323**, 533–536.
- SCHULMAN, JOHN, MORITZ, PHILIPP, LEVINE, SERGEY, JORDAN, MICHAEL & ABBEEL, PIETER 2018 High-dimensional continuous control using generalized advantage estimation, arXiv: 1506.02438.
- SCHULMAN, JOHN, WOLSKI, FILIP, DHARIWAL, PRAFULLA, RADFORD, ALEC & KLIMOV, OLEG 2017 Proximal policy optimization algorithms, arXiv: 1707.06347.
- SEDKY, GIRGUIS, GEMENTZOPOULOS, ANTONIOS, ANDREU-ANGULO, IGNACIO, LAGOR, FRANCIS D. & JONES, ANYA R. 2022 Physics of gust response mitigation in open-loop pitching manoeuvres. *Journal of Fluid Mechanics* **944**, A38.
- THEODORSEN, THEODORE 1949 General theory of aerodynamic instability and the mechanism of flutter. *Tech. Rep.* 496. NACA.
- VASWANI, ASHISH, SHAZEER, NOAM, PARMAR, NIKI, USZKOREIT, JAKOB, JONES, LLION, GOMEZ, AIDAN N., KAISER, LUKASZ & POLOSUKHIN, ILLIA 2017 Attention is all you need. In *Advances in Neural Information Processing Systems*, , vol. 30.
- VERMA, SIDDHARTHA, NOVATI, GUIDO & KOUMOUTSAKOS, PETROS 2018 Efficient collective swimming by harnessing vortices through deep reinforcement learning. *Proceedings of the National Academy of Sciences* **115** (23), 5849–5854.
- WAGNER, HERBERT 1925 Über die entstehung des dynamischen auftriebes von tragflügeln. *Zeitschrift für Angewandte Mathematik und Mechanik* **5** (1), 17–35.
- WANG, Z.P., LIN, R.J., ZHAO, Z.Y., CHEN, X., GUO, P.M., YANG, N., WANG, Z.C. & FAN, D.X. 2024 Learn to flap: foil non-parametric path planning via deep reinforcement learning. *Journal of Fluid Mechanics* **984**, A9.
- WEISSENBACHER, M., BOROVYKH, A. & RIGAS, G. 2025 Reinforcement learning of chaotic systems control in partially observable environments. *Flow, Turbulence and Combustion* .
- WILLIAMS, DAVID R. & KING, RUDIBERT 2018 Alleviating unsteady aerodynamic loads with closed-loop flow control. *AIAA Journal* **56** (6), 2194–2207.
- WU, Z., CAO, Y. & ISMAIL, M. 2019 Gust loads on aircraft. *The Aeronautical Journal* **123** (1266), 1216–1274.
- XIA, CHENGWEI, ZHANG, JUNJIE, KERRIGAN, ERIC C. & RIGAS, GEORGIOS 2024 Active flow control for bluff body drag reduction using reinforcement learning with partial measurements. *Journal of Fluid Mechanics* **981**, A17.